Dalton Transactions

PAPER

View Article Online
View Journal

Cite this: DOI: 10.1039/d6dt00337k

Tuning the crystal structure, optical band gap and persistent luminescence performance of a Cr^{3+}-doped $LiGa_5O_8$ spinel by adding aluminium and indium†

Anastasiia Karabut,[a] Halyna Zhydachevska,[a] Łukasz Wachnicki,[a] Vasyl Hreb,[b] Leonid Vasylechko,*[b] Yuriy Hizhnyi,[c,d] Tetiana Shevtsova,[c] Andriy Luchechko,[e] Agnieszka Pieniążek,[a] Marek Berkowski[a] and Yaroslav Zhydachevskyy*[a,f]

The possibility of tuning the optical band gap, crystal structure and persistent luminescence performance of a Cr^{3+}-doped $LiGa_5O_8$ spinel by partially replacing Ga with Al and/or In has been studied extensively. For this purpose, a series of Cr^{3+}-doped $Li(Ga_{1-x-y}Al_xIn_y)_5O_8$ (x = 0…0.5; y = 0…0.1) microcrystalline phosphors were synthesised using a conventional solid-state reaction method and characterised using powder X-ray diffraction, SEM-EDX and luminescence techniques. DFT-based electronic structure calculations were carried out for the same $Li(Ga_{1-x-y}Al_xIn_y)_5O_8$ compositions, and the results were compared with the experimental ones. Based on the studies performed, the mechanism of Al and In incorporation into the $LiGa_5O_8$ spinel structure as well as the tuning of the crystal lattice parameters, the local structure of M^{3+} (M = Ga, Al, and In) cations and the optical band gap of the material have been established. The multicentre structure and the broadening of the local structural disorder of the octahedrally coordinated Cr^{3+} centres observed in this case have been confirmed by high-resolution, low-temperature photoluminescence measurements. Band gap engineering through alterations in the chemical composition of the $LiGa_5O_8$ spinel, as well as the depth of the native point defects responsible for charge trapping, allows for the efficient tuning of the thermoluminescence and persistent luminescence properties of $Li(Ga_{1-x-y}Al_xIn_y)_5O_8$:$Cr^{3+}$ phosphors. Thus, the room-temperature persistent luminescence performance of the phosphors modified by the addition of Al and annealing under an oxygen-free atmosphere was increased threefold compared to the pristine $LiGa_5O_8$:Cr^{3+} phosphor synthesised under the same conditions.

Received 9th February 2026,
Accepted 20th April 2026

DOI: 10.1039/d6dt00337k

rsc.li/dalton

1. Introduction

A lithium–gallium spinel ($LiGa_5O_8$) activated with rare-earth (RE) or transition metal (TM) ions is a known crystalline phosphor having long-lasting persistent luminescence (PersL) or mechanoluminescence (ML) properties.[1–3] In particular, when activated with Cr^{3+}, it exhibits persistent luminescence in the deep red spectral region at about 700 nm.[4–6] The radiation storage properties allowing the persistent luminescence or mechanoluminescence of the material are caused by intrinsic point defects, such as cation antisites, and cation and oxygen vacancies that are highly probable in this spinel compound.[7–9] These defects reveal themselves through the thermally stimulated luminescence (TSL) that occurs in the material after exposure to UV or higher energy light.

It is well known that the band gap engineering of a crystalline host lattice allows tuning of the TSL and PersL properties of phosphors over a wide range (see *e.g.*, Zhydachevskyy *et al.*).[10] Such a possibility has recently been demonstrated for Ga-containing oxides, such as γ-Ga_2O_3:Cr, by alloying with indium or aluminium oxides.[11] In addition to engineering of the band gap, replacing one host cation with another can also produce disorder in the local structure, thereby broadening the spectral properties of activator ions or intrinsic point defects in the host lattice.[12]

[a]*Institute of Physics, Polish Academy of Sciences, aleja Lotników 32/46, Warsaw 02-668, Poland. E-mail: zhydach@ifpan.edu.pl*
[b]*Lviv Polytechnic National University, S. Bandera Str. 12, Lviv 79013, Ukraine. E-mail: leonid.o.vasylechko@lpnu.ua*
[c]*Donetsk Institute for Physics and Engineering of NAS of Ukraine, Kyiv 03028, Ukraine*
[d]*Taras Shevchenko National University of Kyiv, Volodymyrska Str. 64/13, Kyiv 01601, Ukraine*
[e]*Ivan Franko National University of Lviv, Tarnavskogo Str. 107, Lviv 79017, Ukraine*
[f]*Berdyansk State Pedagogical University, Shmidta Str. 4, Berdyansk 71100, Ukraine*
†The authors dedicate this paper to the memory of our dear friend and colleague Professor Andrzej Suchocki (1953–2025).

Regarding the possibility of tuning the $LiGa_5O_8$ host, not much is known. It is known, however, that the aluminium-based counterpart, $LiAl_5O_8$, has the same type of structure, and a continuous series of $Li(Ga_{1-x}Al_x)_5O_8$ solid solutions exists, which allows for a gradual change in the crystal structure parameters of these spinel compounds.[13,14] At the same time, there is nothing known on the possibility of introducing indium onto either the $LiGa_5O_8$ or $LiAl_5O_8$ compounds to tune the band gap and trap depth in this host. It is also unclear whether the $LiGa_5O_8$ host is optimal for long-lasting PersL and whether it can be improved by modifying the host with aluminium or indium. Therefore, the present work explores the potential of engineering the band gap and local structure to adjust the thermoluminescence and persistent luminescence properties of $Li(Ga,Al,In)_5O_8:Cr^{3+}$ phosphors. For this purpose, a series of $Li(Ga_{1-x-y}Al_xIn_y)_5O_8:Cr^{3+}$ compounds with various compositions (x values ranging from 0 to 0.5 and y values ranging from 0 to 0.1) were synthesised and thoroughly characterised using powder XRD, SEM-EDX and luminescence techniques. DFT-based electronic structure calculations of $Li(Ga_{1-x-y}Al_xIn_y)_5O_8$ alloys with x and y values being the same as in the synthesised samples were carried out to strengthen the inferences obtained from experimental studies.

The electronic structure of the pure $LiGa_5O_8$ spinel has been studied previously by first-principles methods,[15–17] while the electronic properties of native defects in $LiGa_5O_8$ have been studied computationally.[7,8] However, to the best of our knowledge, no results on the electronic structure of $Li(Ga_{1-x-y}Al_xIn_y)_5O_8$ alloys have been published so far.

2. Experimental methods

2.1. Samples and experimental and computational techniques

The studied Cr^{3+}-doped $LiGa_5O_8$-based microcrystalline samples were synthesised using a conventional solid-state reaction technique starting from high-purity Li_2CO_3 (99.99%), Ga_2O_3 (99.99%), Al_2O_3 (99.999%), In_2O_3 (99.999%) and Cr_2O_3 (99.999%) microcrystalline powders. The starting powders were weighed in appropriate proportions corresponding to the lithium-rich composition of $Li_{1.02}Ga_5O_8$ and thoroughly ground in an agate mortar. The 2% excess of Li_2CO_3 was proven experimentally to be the optimal composition for obtaining the single-phase spinel under the given synthesis conditions. Specifically, when the stoichiometric ratio of Li_2CO_3 and Ga_2O_3 was used, alongside the main $LiGa_5O_8$ spinel, residual traces of γ-Ga_2O_3 were observed in the final products. The Cr_2O_3 dopant at a concentration 0.5 mol% was added at the expense of Li_2CO_3 (which was already in excess). The same mixture of 99.5% Li_2CO_3 + 0.5% Cr_2O_3 prepared in a larger amount was used for preparing all the Cr-doped samples to ensure the same chromium concentration in the samples (see Table 1). The final mixtures were pre-synthesised at 800 °C for 2 hours, then thoroughly ground once more in an agate mortar and finally synthesised at 1300 °C for 3 hours. Both the preliminary and final syntheses were performed in alundum crucibles under normal air conditions.

Additionally, in order to study the effect of reducing annealing, the samples were annealed under high vacuum at 1000 °C for 2 hours. For this, a part of each powder sample was annealed in alundum crucibles in a closed quartz reactor that was continuously pumped out up to a pressure of 10^{-5} mbar.

X-ray powder diffraction (XRD) characterization of the synthesised materials was performed using an Aeris benchtop powder diffractometer (Malvern Panalytical) equipped with a PIXcel^{1D} strip detector. Experimental diffraction data were collected using filtered Cu K_α radiation (λ = 1.54185 Å) in a 2θ range of 6–105 degrees with a 2θ step of 0.02°. Lattice parameters, coordinates and displacement parameters of atoms were derived from the experimental XRD patterns by full profile Rietveld refinement using the WinCSD software package.[18]

Scanning electron microscopy (SEM) and energy-dispersive X-ray spectroscopy (EDX) analyses were carried out using a Hitachi SU-70 scanning electron microscope coupled with a Thermo Fisher Scientific energy dispersive X-ray spectrometer with a Li-drift silicon X-ray detector.

The photoluminescence (PL) and the photoluminescence excitation (PLE) spectra were recorded using a Horiba/Jobin–Yvon Fluorolog-3 spectrofluorometer with a 450 W continuous spectrum xenon lamp for excitation. The emission was detected using a Hamamatsu R928P photomultiplier operating in photon counting mode. The PL spectra were corrected for the spectral response of the used system. The afterglow (PersL) decay kinetics and the thermally stimulated luminescence (TSL) curves were measured using the same Fluorolog-3 spectrofluorometer in real-time decay mode. TSL measurements in the temperature range of 77–700 K were performed using a Linkam THMS600 temperature stage with linear heating at a rate of 1 K s^{-1}. Photoluminescence quantum efficiency measurements were performed using the same spectrofluorometer and a Horiba Quant-phi integrating sphere. The quantum efficiency (QE) was calculated as the ratio of the number of emitted photons to that of the absorbed photons similarly as it is described in the work of Zhydachevskyy *et al.*[19] PLE measurements using synchrotron radiation were performed using the facilities of PETRA III P66 beamline of the Deutsches Elektronen-Synchrotron DESY, Hamburg, Germany.[20]

DFT-based electronic structure calculations of $Li(Ga_{1-x-y}Al_xIn_y)_5O_8$ alloys were performed using the supercell approach. The supercells were constructed by 2 × 2 × 2 replication of the unit cell of the $Li(Ga_{1-x-y}Al_xIn_y)_5O_8$ crystal, resulting in a structure containing 448 atoms (Fig. S4). All supercells were assigned the primitive symmetry group $P1$. The number of cationic substitutions modelled in the supercells for each x and y is listed in Table S1. For each x and y, 10 structures were generated with random distributions of In_{Ga} and Al_{Ga} substitutions. All structures were subjected to geometrical optimisation, and the total energies were calculated for each configuration. The optical spectra were calculated only for the

Table 1 List of the Cr^{3+}-doped $Li(Ga_{1-x-y}Al_xIn_y)_5O_8$ samples studied

Sample notation	Composition Chemical formula	Al content (%)	In content (%)	Phase composition
0% Al	$LiGa_5O_8$:Cr(0.5%)	0	0	Pure spinel
5% In	$Li(Ga_{0.95}In_{0.05})_5O_8$:Cr(0.5%)	0	5	Almost pure spinel
10% In	$Li(Ga_{0.9}In_{0.1})_5O_8$:Cr(0.5%)	0	10	Spinel + γ-(Ga,In)O_3
5% Al	$Li(Ga_{0.95}Al_{0.05})_5O_8$:Cr(0.5%)	5	0	Pure spinel
10% Al	$Li(Ga_{0.9}Al_{0.1})_5O_8$:Cr(0.5%)	10	0	Pure spinel
5% Al 5% In	$Li(Ga_{0.9}Al_{0.05}In_{0.05})_5O_8$:Cr(0.5%)	5	5	Pure spinel
7% Al 3% In	$Li(Ga_{0.9}Al_{0.07}In_{0.03})_5O_8$:Cr(0.5%)	7	3	Pure spinel
14% Al 6% In	$Li(Ga_{0.8}Al_{0.14}In_{0.06})_5O_8$:Cr(0.5%)	14	6	Spinel + γ-(Ga,In)O_3
20% Al	$Li(Ga_{0.8}Al_{0.2})_5O_8$:Cr(0.5%)	20	0	Pure spinel
30% Al	$Li(Ga_{0.7}Al_{0.3})_5O_8$:Cr(0.5%)	30	0	Pure spinel
40% Al	$Li(Ga_{0.6}Al_{0.4})_5O_8$:Cr(0.5%)	40	0	Pure spinel
50% Al	$Li(Ga_{0.5}Al_{0.5})_5O_8$:Cr(0.5%)	50	0	Pure spinel

structures with the lowest total energy among all configurations modelled for each x and/or y value.

Electronic structure calculations were performed using the DFT-based band-periodic pseudopotential method implemented in the CASTEP program, which is part of the Materials Studio package.[21] Geometry optimisation accounted for the exchange–correlation effects using the GGA–PBE approximation.[22] Atomic positions were optimised using the Broyden–Fletcher–Goldfarb–Shanno (BFGS) minimization algorithm[23] with the convergence criterion for energy and force on the atoms, which were set to 10^{-5} eV per atom and 0.03 eV per Å per atom, respectively. Geometry optimizations were performed only for the Γ point of the Brillouin zone.

To overcome the underestimation of the band gap energies E_g using the PBE functional, the optical (inter-band) absorption spectra were calculated using the GGA–PBE plus Hubbard U (GGA+U) approach.[24] The on-site Coulomb corrections (U) for specific orbitals (O 2p: 6.7 eV, Ga 3d: 7.0 eV, Al 3d: 7.0 eV, and In 3d: 5.0 eV) were selected from the conditions of the best agreement between the calculated and experimental band gaps for Ga_2O_3, Al_2O_3 and In_2O_3 crystals (see details in Vasylechko *et al.*).[25]

For the calculations of the optical absorption spectra, the Brillouin zone was sampled using a 2 × 2 × 2 k-point grid.

3. Results and discussion

3.1. Phase composition and crystal structure

All the synthesised $LiGa_5O_8$-based samples presented in Table 1 show a pure cubic spinel structure (Fig. 1a). Only in the materials of nominal compositions $Li(Ga_{0.9}In_{0.1})_5O_8$ and $Li(Ga_{0.8}Al_{0.14}In_{0.06})_5O_8$ with a relatively higher indium content, the traces of γ-(Ga,In)O_3 mixed oxide could be detected. Left- and right-side shifts of the Bragg's maxima of the In- and Al-substituted samples (see Fig. 1b) indicate the successful and progressive incorporation of both these ions into the $LiGa_5O_8$ structure.

More deep examination of the experimental XRD profiles of the $Li(Ga_{1-x}Al_x)_5O_8$ series revealed significant and progressive peak broadening with increasing Al content (Fig. 1b), caused by a drastic increase of the microstrain values $\langle\varepsilon\rangle$ in these mixed spinel materials from 0.01–0.02% for nominally pure $LiGa_5O_8$ and x = 0.05 sample to 0.19–0.24% for the Al-richest samples with x = 0.4 and 0.5, as it was further derived by full profile Rietveld refinement. This is obviously caused by an increase in the dispersion of interplanar distances with increasing Al content in the $Li(Ga_{1-x}Al_x)_5O_8$ series.

To shed light on the peculiarities of cation substitution in the $LiGa_5O_8$ spinel structure, precise structural analysis was performed using the full profile Rietveld refinement technique. As a starting model for the refinement, atomic positions in the prototype $LiFe_5O_8$ spinel structure derived from the X-ray single crystal data of Tomas *et al.*[26] were used. After adjusting the lattice parameters along with corrections of instrumental sample shifts, the atomic coordinates and displacement parameters (adp's) of atoms were refined. For the unsubstituted $LiGa_5O_8$:Cr material, the excellent fit and very low residuals of R_I = 0.0277 and R_P = 0.0407 were obtained (see Table 2). In the case of $Li(Ga_{1-x}Al_x)_5O_8$:Cr series, structural refinement using different combinations of metal cations in the two non-equivalent Ga sites showed that the better fit with the lowest residuals and physically reliable values of adp's (see Fig. S1 and Table 2) were achieved assuming the mixed occupancy of the octahedral Ga1 position with Ga^{3+} and Al^{3+} ions, whereas the tetrahedral position of Ga2 atoms remains occupied mainly with gallium. In contrast, for the indium-substituted $Li(Ga_{0.95}In_{0.05})_5O_8$:Cr and $Li(Ga_{0.9}In_{0.1})_5O_8$:Cr samples, better results were achieved assuming that In^{3+} ions partially replace gallium in the Ga2 tetrahedral sites of the $LiGa_5O_8$ spinel structure (Table 2). This rather unexpected result was further corroborated by analysis of the obtained structural information; in particular, evolution of the average bond lengths inside two kinds of polyhedra *vs.* the substitution level in the $Li(Ga_{1-x}Al_x)_5O_8$ and $Li(Ga_{1-x}In_x)_5O_8$ spinel structures (see below). Structural refinement of the doubly substituted $Li(Ga_{0.9}Al_{0.05}In_{0.05})_5O_8$ and $Li(Ga_{0.9}Al_{0.07}In_{0.03})_5O_8$ materials using different combinations of metal cations in the two non-equivalent Ga sites showed that the lowest residuals and physically reliable values of adp's were achieved when the octahedral Ga1 position in the spinel structure is occupied with a mixture of Ga^{3+} and Al^{3+} ions, while the tetrahedral 8c site contains Ga^{3+} and In^{3+} species (see Fig. S1 and Table 2).

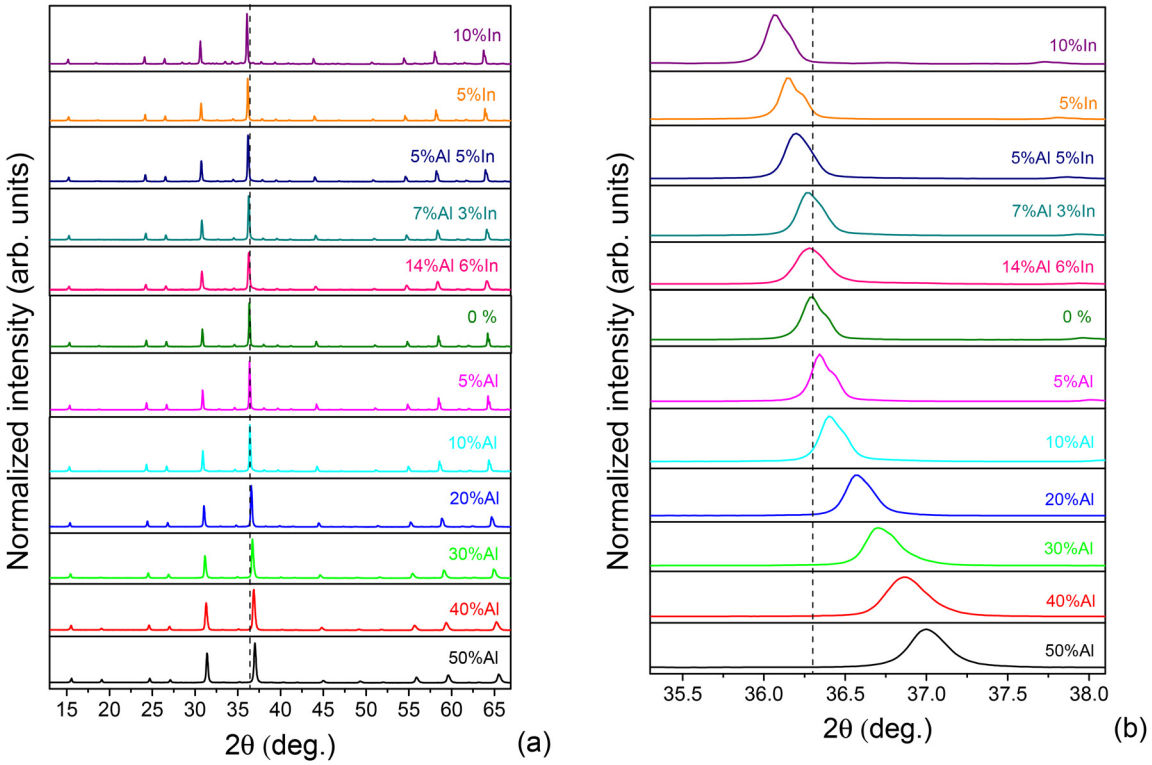

Fig. 1 Fragments of the XRD patterns of the Cr-doped $LiGa_5O_8$-based materials. The vertical dashed lines serve as a guide for the eyes for tracking the changes in the position of Bragg's maxima due to a partial substitution of gallium ions with aluminium and/or indium species in the $LiGa_5O_8$ structure.

The refined structural parameters and atomic occupancy of nominally pure $LiGa_5O_8$, four representatives of Al- and In-substituted spinels and the double substituted $Li(Ga_{0.9}Al_{0.05}In_{0.05})_5O_8$ material are summarised in Table 2.

$LiGa_5O_8$ belong to the $LiFe_5O_8$ type of structure, a 1 : 3 ordered variant of the inverse spinel structure with gallium both in the tetrahedral and octahedral sites and Li ions in the octahedral environment, according to the notation $Ga_2(LiGa_3)O_8$. Fig. 2 shows polyhedral visualisation of the crystal structure of $Li(Ga_{1-x-y}Al_xIn_y)_5O_8$ solid solutions, in which Al^{3+} and In^{3+} ions partially replace the Ga^{3+} ions in the octahedral 12*b* and tetrahedral 8*c* sites, respectively. Both GaO_6 octahedra and GaO_4 tetrahedra in the $LiGa_5O_8$ structure are not regular, as it was reported in ref. 13 and 14, but considerably distorted both in terms of the variation of intrapolyhedral Ga–O distances (see Fig. 2, right panel) and the deviations of O–Ga–O bond angles from the ideal values of 90 and 109.47 degrees, respectively (see the corresponding section below). In spite of six nearest Li–O distances in the $LiGa_5O_8$ structure are all equal, the LiO_6 octahedra are not fully regular due to the detectable deviation of O–Li–O bond angles from 90 degrees (see the section below).

The analysis of the structural results shows that the lattice parameters of both mixed spinel series demonstrate the expected opposite behaviour with an increase in the cation substitution level, a systematic linear decrease in the Li $(Ga_{1-x}Al_x)_5O_8$ materials and clear increase in the case of Li $(Ga_{1-x}In_x)_5O_8$ samples (Fig. 3, left panel), which corresponds to the tabulated ionic radii of the Ga^{3+} ion of the host $LiGa_5O_8$ structure and the substituting Al^{3+} and In^{3+} species, respectively.[27] For the doubly substituted $Li(Ga_{1-x-y}Al_xIn_y)_5O_8$ samples, the lattice parameters lie between the Al- and In-substituted series.

The peculiarities of cation substitution in the two investigated series can be noted when considering the nearest cation–oxygen environment in the corresponding structures (Fig. 3, right panel). Increasing Al content in the Li $(Ga_{1-x}Al_x)_5O_8$ series mainly affects the average M–O distances within the $(Ga,M)O_6$ octahedra, which start to gradually decrease from $x = 0.1$, while the average bond lengths inside the $(Ga,M)O_4$ tetrahedra remain practically unchanged. In contrast, in the $Li(Ga_{1-x}In_x)_5O_8$ materials, the entry of In into the host $LiGa_5O_8$ structure causes a pronounced increase in the average bond lengths inside the $(Ga,M)O_4$ tetrahedra without noticeable changes in the intraoctahedral distances. This observation confirms the above conclusion obtained from the Rietveld refinement that aluminium ions prefer to occupy the octahedral 12*b* position in the $Li(Ga_{1-x}Al_x)_5O_8$ structures, whereas large indium cations mainly occupy the 8*c* Ga tetrahedral site in the $Li(Ga_{1-x}In_x)_5O_8$ structures.

Examination of the nearest environment of the Li ions in the 4*b* site, which are surrounded by six equidistance oxygen

Table 2 Lattice parameters, fractional coordinates and displacement parameters of atoms in the structures of the 0.5% Cr-doped $LiGa_5O_8$-based spinel materials (SG $P4_332$, $Z = 4$)

Atoms, sites	x/a	y/b	z/c	$B_{iso/eq}$, Å^2	Occupancy
$LiGa_5O_8$: a = 8.20421(5) Å; R_I = 0.0277, R_P = 0.0407					
Li, 4*b*	5/8	5/8	5/8	0.61(13)	Li^{+} [a]
Ga1, 12*b*	1/8	0.36562(3)	$-y + 1/4$	0.916(7)	1.002(2) Ga^{3+}
Ga2, 8*c*	−0.00360(4)	x	x	0.832(8)	1.001(1) Ga^{3+}
O1, 8*c*	0.3865(2)	x	x	0.95(4)	0.999(2) O^{2-}
O2, 24*e*	0.1200(2)	0.1286(1)	0.3854(1)	1.25(2)	0.999(2) O^{2-}
$Li(Ga_{0.95}Al_{0.05})_5O_8$: a = 8.19413(6) Å; R_I = 0.0260, R_P = 0.0501					
Li, 4*b*	5/8	5/8	5/8	0.9(2)	Li^{+} [a]
Ga1, 12*b*	1/8	0.36561(4)	$-y + 1/4$	1.21(1)	0.974(5) Ga^{3+} + 0.026(5) Al^{3+}
Ga2, 8*c*	−0.00412(4)	x	x	0.91(1)	1.001(5) Ga^{3+} + 0.001(5) Al^{3+}
O1, 8*c*	0.3878(2)	x	x	1.67(7)	0.999(2) O^{2-}
O2, 24*e*	0.1216(2)	0.1283(2)	0.3829(2)	1.28(4)	0.997(2) O^{2-}
$Li(Ga_{0.5}Al_{0.5})_5O_8$: a = 8.0569(2) Å; R_I = 0.0318, R_P = 0.0789					
Li, 4*b*	5/8	5/8	5/8	0.8(2)	Li^{+} [a]
Ga1, 12*b*	1/8	0.36855(8)	$-y + 1/4$	1.12(2)	0.203(2) Ga^{3+} + 0.797(2) Al^{3+}
Ga2, 8*c*	−0.00251(6)	x	x	1.346(9)	0.952(3) Ga^{3+} + 0.048(3) Al^{3+}
O1, 8*c*	0.3847(2)	x	x	2.30(7)	0.999(3) O^{2-}
O2, 24*e*	0.1091(2)	0.1311(1)	0.3870(2)	1.42(3)	1.000(2) O^{2-}
$Li(Ga_{0.95}In_{0.05})_5O_8$: a = 8.23558(6) Å; R_I = 0.0275, R_P = 0.0582					
Li, 4*b*	5/8	5/8	5/8	0.7(2)	Li^{+} [a]
Ga1, 12*b*	1/8	0.36583(4)	$-y + 1/4$	0.94(1)	1.000(6) Ga^{3+} + 0.000(6) In^{3+}
Ga2, 8*c*	−0.00304(5)	x	x	0.90(1)	0.931(6) Ga^{3+} + 0.069(6) In^{3+}
O1, 8*c*	0.3856(3)	x	x	1.50(7)	0.996(3) O^{2-}
O2, 24*e*	0.1150(2)	0.1270(2)	0.3878(2)	1.35(3)	0.998(2) O^{2-}
$Li(Ga_{0.9}Al_{0.05}In_{0.05})_5O_8$: a = 8.22835(8) Å; R_I = 0.0265, R_P = 0.0560					
Li, 4*b*	5/8	5/8	5/8	0.7(2)	Li^{+} [a]
Ga1, 12*b*	1/8	0.36580(4)	$-y + 1/4$	0.820(9)	0.960(6) Ga^{3+} + 0.040(6) Al^{3+}
Ga2, 8*c*	−0.00325(4)	x	x	0.932(10)	0.860(5) Ga^{3+} + 0.140(5) In^{3+}
O1, 8*c*	0.3898(2)	x	x	0.63(6)	0.998(3) O^{2-}
O2, 24*e*	0.1182(2)	0.1294(2)	0.3863(2)	1.22(2)	0.998(2) O^{2-}

[a] Fixed at unity.

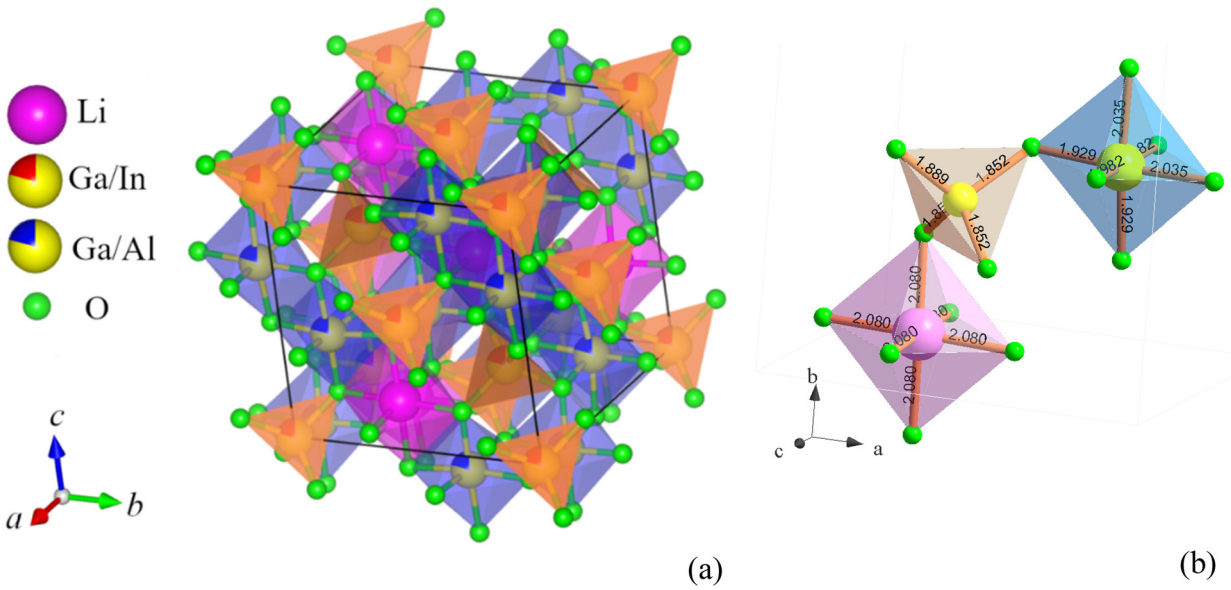

Fig. 2 Vesta plot of the $Li(Ga_{1-x-y}Al_xIn_y)_5O_8$ crystal structure showing the preferred location of substituting Al and In ions in the octahedral Ga1 and tetrahedral Ga2 positions of the 1 : 3 ordered inverse spinel structure (a) and the configuration of three types of coordination polyhedra in the parent $LiGa_5O_8$ structure (b).

ions, revealed a sudden discontinuity at $x = 0.2$ against a background of a downward trend with increasing x in the Li $(Ga_{1-x}Al_x)_5O_8$ series. This observation indicates that a partial inclusion of the smallest Al ions on the octahedral position of Li ions in the 4*b* site could not be neglected. A similar phenomenon, *i.e.* mixed occupancy of the octahedral 4*b* site

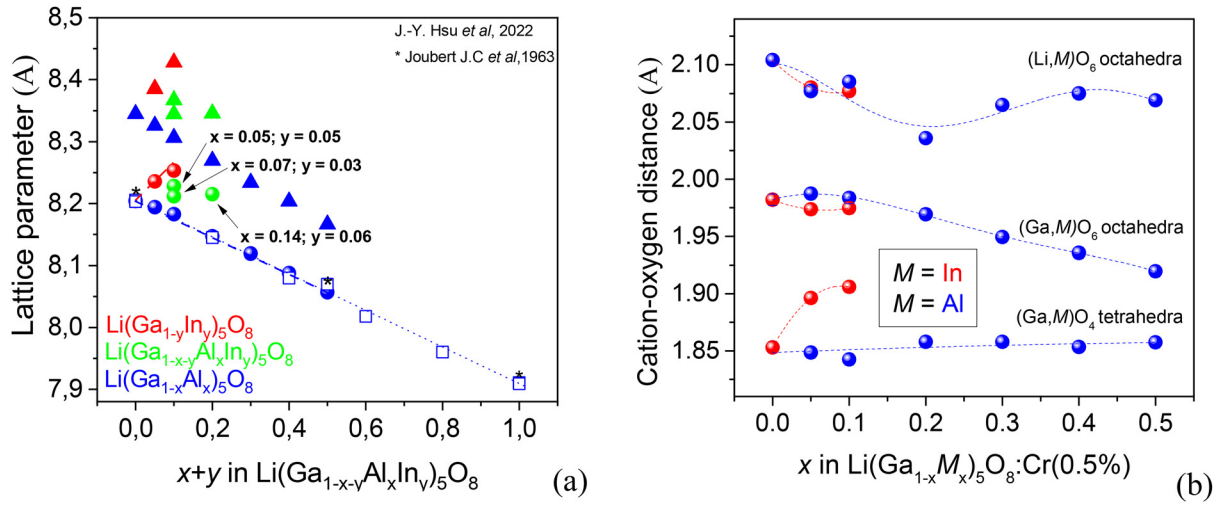

Fig. 3 Concentration dependence of the calculated (triangles) and experimental (circles) lattice parameters (a) and average Ga–O interatomic distances (b) in the $Li(Ga_{1-x}Al_x)_5O_8$ and $Li(Ga_{1-x}In_x)_5O_8$ series (blue and red spheres, respectively). The open squares and the asterisks denote the lattice parameters taken from ref. 13 and 28, respectively. The dashed lines show polynomial fits for a guide to the eyes.

with Li and Fe ions in the prototyping $LiFe_5O_8$ structure, was reported by Tomas *et al.*[26] Unfortunately, negligible scattering factor of lithium ions does not allow to refine adequately a possible mixed occupancy of the 4*b* site with different metal ions in $Li(Ga_{1-x}Al_x)_5O_8$ from the X-ray diffraction data.

Deeper analysis of the structural parameters of the $Li(Ga_{1-x}Al_x)_5O_8$ series allows us to reveal several interesting features in the concentration behaviour of the individual interatomic distances inside three different coordination polyhedra, tetrahedra GaO_4 and octahedra GaO_6 and LiO_6 (Fig. 4, green, red and blue symbols, respectively). All these distances show a detectable decreasing tendency due to the overall lattice contraction of $Li(Ga_{1-x}Al_x)_5O_8$ series and exhibit clear discontinuity between x = 0.1 and 0.2. Three different Ga–O distances inside the GaO_6 octahedra, after its initial approach at x = 0.1, begin to progressively divergence with further increasing Al content. In contrast, two distinct distances within the GaO_4 tetrahedra (one Ga–O1 and three Ga–O2) display a clear con-

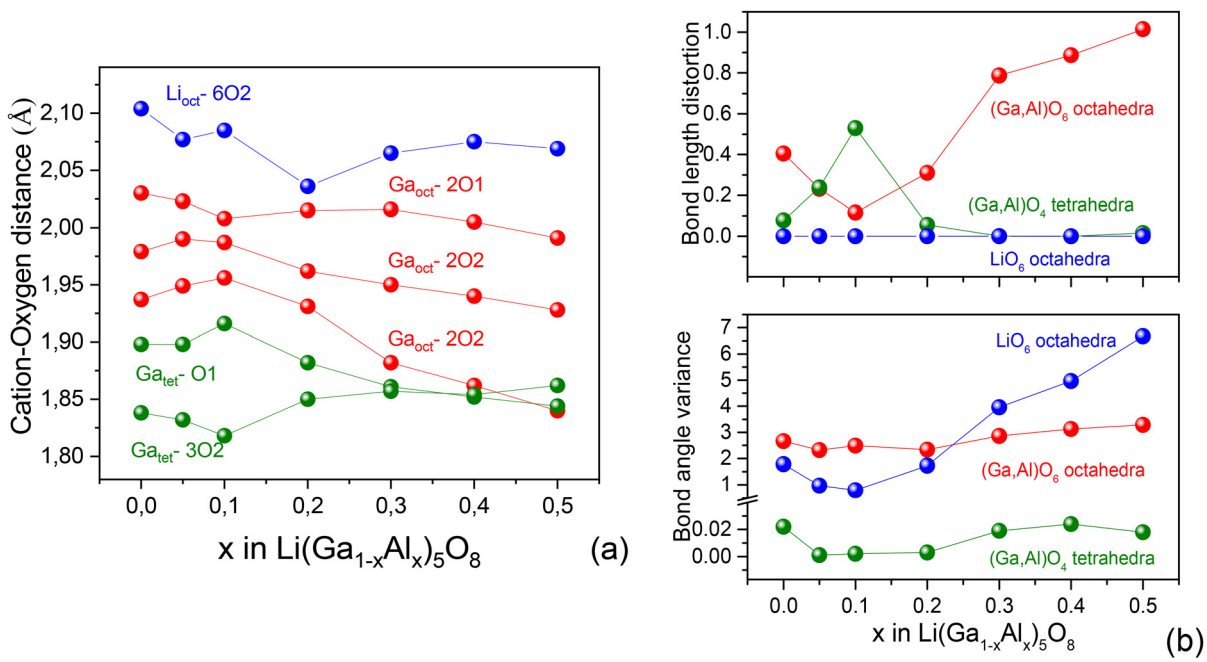

Fig. 4 Concentration evolution of the nearest cation–oxygen distances (a) and bond length distortion in the tetrahedral and two octahedral positions of metal ions (b) in the $Li(Ga_{1-x}Al_x)_5O_8$ series.

vergence behaviour after $x = 0.1$, becoming practically equal at $x = 0.3$ and 0.4 (see Fig. 4).

The observed deviations from the regular trends of Ga–O distances in the GaO_6 octahedra and the GaO_4 tetrahedra are manifested in the corresponding bond length distortion parameters calculated according to Sasaki *et al.*[29] as:

$$\Delta = \frac{1}{n}\sum\left(\frac{l_i - l_{CN}}{l_{CN}}\right)^2 \times 10^3, \quad (1)$$

where l_i and l_{CN} are the individual and average interatomic distances in the polyhedra with the corresponding coordination number and n is the number of bonds. Clear extrema in the bond length distortion – a minimum for the GaO_6 octahedra and the maximum for the GaO_4 tetrahedra (Fig. 4, right top panel) – reflect the complex character of cation substitution in the $Li(Ga_{1-x}Al_x)_5O_8$ series. Since the six Li–O distances inside the LiO_6 octahedra are equal due to the symmetry of the 4*b* site, there is no bond length distortion ($\Delta = 0$). However, the LiO_6 octahedra cannot be considered as regular due to the deviation of bond angles inside the octahedra from 90 degrees. Bond angle distortion (variance) in the coordination polyhedra, σ, can be calculated similarly to bond length distortion: $\sigma = 1/n\Sigma((\varphi - \varphi_i)/\varphi_i)^2$. It stands as a measure of deviation of the actual bond angle φ from the ideal values φ_i for the corresponding polyhedra (90° for octahedra and 109.47° for tetrahedra). Evolution of calculated values for the three distinguished polyhedra in the $Li(Ga_{1-x}Al_x)_5O_8$ series is presented on the right bottom panel in Fig. 4. As for the bond angle dispersion σ, LiO_6 octahedra with six equal Li–O internal distances are considerably distorted and the unevenly increasing evolution *vs.* Al content with a noticeable deflection at $x = 0.1$ reflects the complex scenario of cation substitution in the Li $(Ga_{1-x}Al_x)_5O_8$ series. Bond angle variance in the GaO_6 octahedra and GaO_4 tetrahedra depends weakly on the Li $(Ga_{1-x}Al_x)_5O_8$ composition, in contrast to bond length distortion, showing clear opposite extrema at $x = 0.1$ (Fig. 4, right panel).

XRD examination of the same samples, annealed in a high vacuum at 1000 °C for 2 hours, revealed no detectable changes in the phase compositions and crystal structure parameters of the studied materials. Illustrative pictures from full profile Rietveld refinement proving phase purity and crystal structure of the $Li(Ga_{1-x}Al_x)_5O_8$, and $Li(Ga_{1-x}In_x)_5O_8$ Li $(Ga_{0.9}Al_{0.05}In_{0.05})_5O_8$ spinel materials after their reducing annealing are presented in Fig. S2. Refined structural parameters of these samples practically do not differ from the initial air annealed materials and show very similar concentration behaviour with increasing cation substitution level in the $Li(Ga_{1-x}Al_x)_5O_8$ and $Li(Ga_{1-x}In_x)_5O_8$ series (see Fig. S3).

3.2. Microstructure and elemental composition

SEM imaging of the studied samples testifies that they have a strongly agglomerated microstructure, as shown in Fig. 5. It is noteworthy that the non-modified $LiGa_5O_8$ and In-containing $Li(Ga_{0.95}In_{0.05})_5O_8$ samples have a typical size of the microcrystalline grains of ≥1 μm, while the Al-containing samples have smaller grains of up to 0.5 μm or even smaller for the Li $(Ga_{0.5}Al_{0.5})_5O_8$ sample.

EDX elemental analysis and mapping (see Fig. 6) confirm a uniform distribution of Ga, Al and In elements within the grains of the single-phase samples. At the same time, the Cr distribution in the maps is barely noticeable, obviously because of its low content (0.5 at% with respect to Li), while its presence has been confirmed by a quantitative analysis of the EDX spectra.

3.3. DFT calculations

The calculated total energies E for all sets of $Li(Ga_{1-x}Al_x)_5O_8$ supercells are presented in Fig. 7. For each x value, the origin of the energy scale is chosen at the calculated E value of the lowest-energy structure. For each x, 10 structures were created with random location of Al over Ga positions, with Al_{Ga} randomly distributed between the octahedral and tetrahedral cationic sites (see section 3.1 for details). The number of Al_{Ga} at the tetrahedral positions is shown in Fig. 7 for each energy level corresponding to one such structure.

As Fig. 7 clearly shows, the greater the number of Al_{Ga} at tetrahedral positions in the structure, the greater its calculated total energy, and this trend is observed for all x values considered in calculations. Analysing the data presented in Fig. 7, it can be approximately assumed that when one additional Al_{Ga} cation is placed in any tetrahedral position of the lattice while maintaining the total amount of Al_{Ga} (*i.e.*, the value of x), the total energy of the structure increases by an average of 0.5–1 eV. From this fact, we can conclude that, regardless of the value of x, the most energetically favourable structures of $Li(Ga_{1-x}Al_x)_5O_8$ (x from 0 to 0.5) will be those in which all Al_{Ga} is at the octahedral positions of the lattice.

As established from the experimental results (see 3.1 section), Al_{Ga} substitutions preferentially occur at the octahedral Ga sites. Our calculations definitely confirm this suggestion.

At the same time, from the experimental results, it was suggested that the In_{Ga} substituents preferentially occupy octahedral Ga sites (see section 3.1). This conclusion is also confirmed by our calculations. As can be seen in Fig. 8, the greater the number of In_{Ga} at the octahedral sites in the structure, the higher its energy.

Taking into account the above results, optical spectral calculations were performed for the $Li(Ga_{1-x-y}Al_xIn_y)_5O_8$ supercells in which the Al_{Ga} substituents were situated only in the octahedral positions, and In_{Ga} in the tetrahedral ones. The lattice parameters of $Li(Ga_{1-x-y}Al_xIn_y)_5O_8$ obtained from DFT geometry optimizations of the supercells with the lowest-energy structures, in which Al_{Ga} randomly occupies octahedral positions and In_{Ga} occupies tetrahedral positions, are presented in Fig. 3 (see section 3.1) and also listed in Table S2. Although DFT-based optimizations usually slightly overestimate the unit cell volumes (and the corresponding lattice constants), our calculations clearly reproduce the experimentally

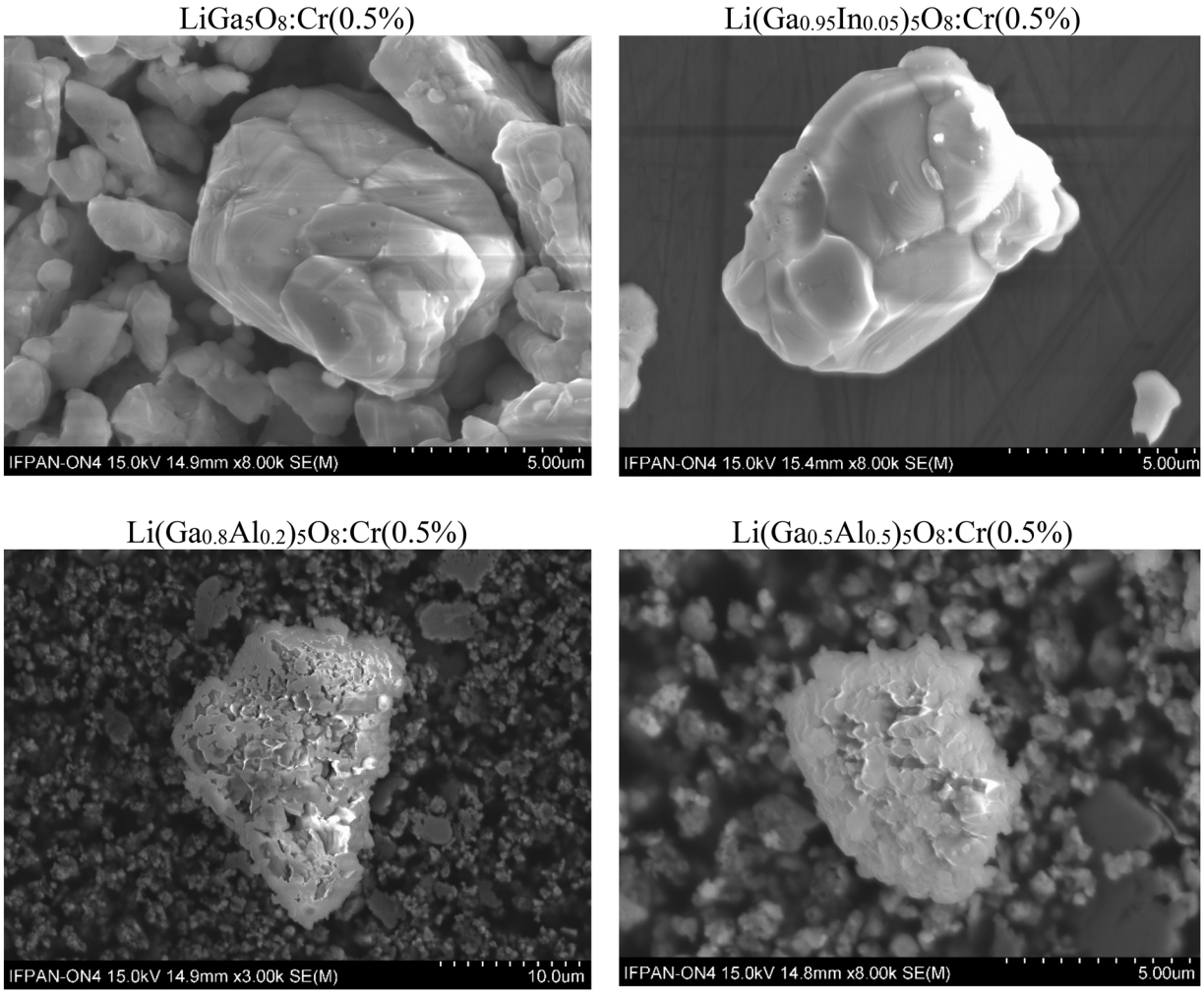

Fig. 5 High-resolution SEM images of the selected samples studied.

observed trends obtained for the synthesised set of Li$(Ga_{1-x-y}Al_xIn_y)_5O_8$ samples.

Using calculations of the optical spectra of the lowest-energy Li$(Ga_{1-x-y}Al_xIn_y)_5O_8$ structures, we evaluated the trends in the crystal band gaps depending on the cation composition of the compound.

Dependencies of the calculated absorption spectra of Li$(Ga_{1-x-y}Al_xIn_y)_5O_8$ alloys on the values of x and y are shown in Fig. S5. From these data, we estimated the energies at which the absorption coefficient of the Li$(Ga_{1-x-y}Al_xIn_y)_5O_8$ alloy with specific x and y reaches the value of $\sim 10^4$ cm^{-1}, which has a pure $LiGa_5O_8$ crystal at energy of 4.9 eV (as it will be shown in the next section, this energy may reflect the onset of excitonic or band-to-band PL excitation). Using these energy points, we approximately estimate the shifts of the spectra of the alloys relative to the pure crystal. Although the spectra were obtained in approximate calculations, such shifts obviously have to correlate with changes in the energy gaps E_g of Li$(Ga_{1-x-y}Al_xIn_y)_5O_8$ compounds depending on the cation content.

If we presumably approximate the value of E_g of the pure $LiGa_5O_8$ crystal as 4.9 eV (the actual value probably may be 0.2–0.5 eV higher),[30] according to the above analysis of the calculation results, the trends in the energy gaps should be as shown in Fig. 9.

As shown in Fig. 9, doping with 50% of Al increases the E_g value of $LiGa_5O_8$ by almost 1 eV. Indium doping, and in contrast, reduces the band gap, and this reduction has more pronounced concentration dependence: 10% of Al in the alloy increases its *Eg* by only 0.17 eV, while 10% of In reduces it by 0.30 eV. In addition, as can be seen from the figure (see the green dots), simultaneous doping with Al and In (in concentrations of 5% Al + 5% In and 14% Al + 6% In) practically does not change the band gap of the $LiGa_5O_8$ crystal. There is clear correlation between the band gap energy and the lattice parameters (unit cell volume) of Li$(Ga_{1-x-y}Al_xIn_y)_5O_8$ solid solutions: the smaller the unit cell volume in the Li$(Ga_{1-x}Al_x)_5O_8$ series – the wider the band gap, and the larger the volume of the unit cell in the Li$(Ga_{1-x}In_x)_5O_8$ series – the narrower the band gap (comparison of Fig. 3 and 9). A similar effect has recently been

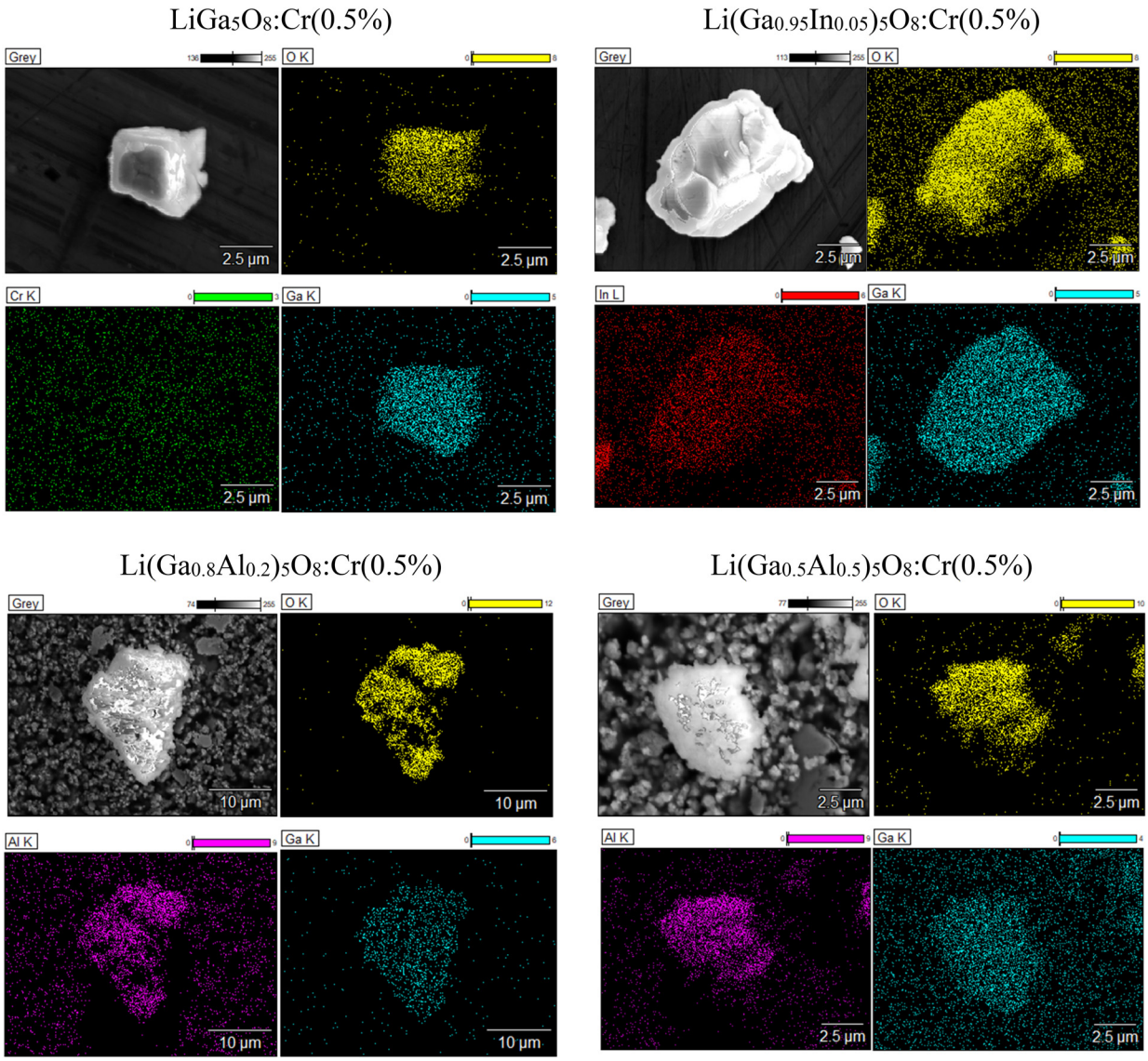

Fig. 6 EDX maps of the selected samples studied.

observed for the aluminium- and indium-substituted β-Ga_2O_3-based solid solutions with a monoclinic structure.[25]

Thus, the results of our calculations show the possibility of band gap engineering of $Li(Ga_{1-x-y}Al_xIn_y)_5O_8$ compounds: the E_g value can be significantly increased by Al doping, decreased by In doping, and maintained at the same level by co-doping Al and In in a certain proportion.

3.4. Photoluminescence

The room-temperature PL and the corresponding PLE spectra of the studied samples are shown in Fig. 10 and 11. These results reveal the characteristic spectra of Cr^{3+} centres in an octahedral coordination.[31] In particular, the excitation bands at about 600 and 400 nm are caused by the spin-allowed $^4A_2 \rightarrow {}^4T_2$ (^4F) and $^4A_2 \rightarrow {}^4T_1$ (^4F) transitions of Cr^{3+}, respectively, while the third excitation band at about 300 nm is related most probably to the $^4A_2 \rightarrow {}^4T_2$ (^4P) transition of Cr^{3+} and/or the charge transfer (CT) transitions with the participation of Cr^{3+} (see *e.g.*, Stasiv *et al.*).[11] Above these excitation bands, an edge-like excitation caused by the band-to-band transitions in the host lattice is observed. It is noteworthy that upon partial substitution of gallium by aluminium, the 600 and 400 nm excitation bands shift towards higher energies, and conversely, when Ga is replaced by In, a red shift of these bands is observed. This behaviour is consistent with the results reported previously[11,13,32] and arises from the alteration in crystal field strength experienced by Cr^{3+} ions due to the replacement of Ga ions by Al or In. A larger shift of the edge-like and the CT excitation bands is obviously caused by the alteration in the band gap of the host lattice (see also Fig. 9 and Fig. S7). As one can see from Fig. 9, the shift of the excitation edge related to band-to-band transitions (which characterises

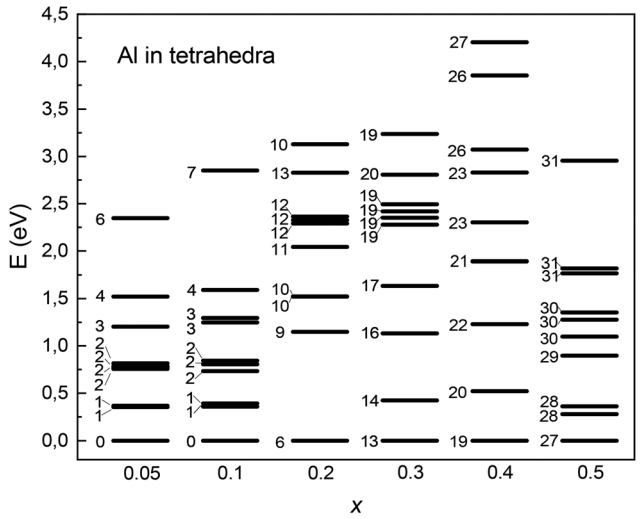

Fig. 7 Calculated total energies of the $Li(Ga_{1-x}Al_x)_5O_8$ supercells with varying atomic structures grouped by the same x. The number of Al_{Ga} substituents occupying the tetrahedral sites are indicated for each supercell.

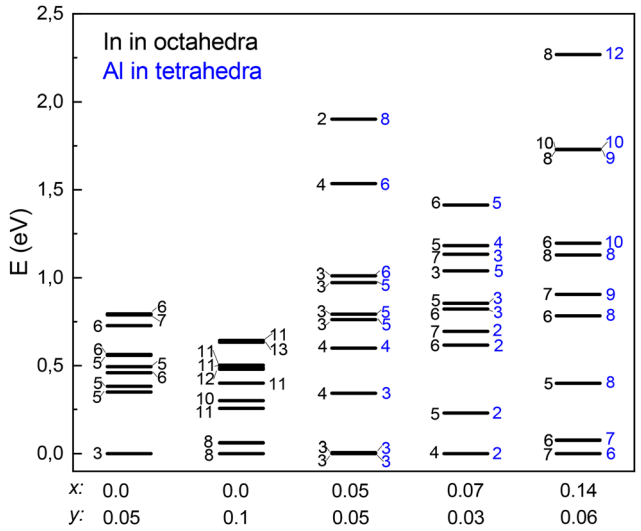

Fig. 8 Calculated total energies of the $Li(Ga_{1-x-y}Al_xIn_y)_5O_8$ supercells with varying atomic structures grouped by the same x and y. The number of In_{Ga} substituents in the octahedral sites are indicated by black numbers and the number of Al_{Ga} substituents in the tetrahedral sites are indicated by blue ones.

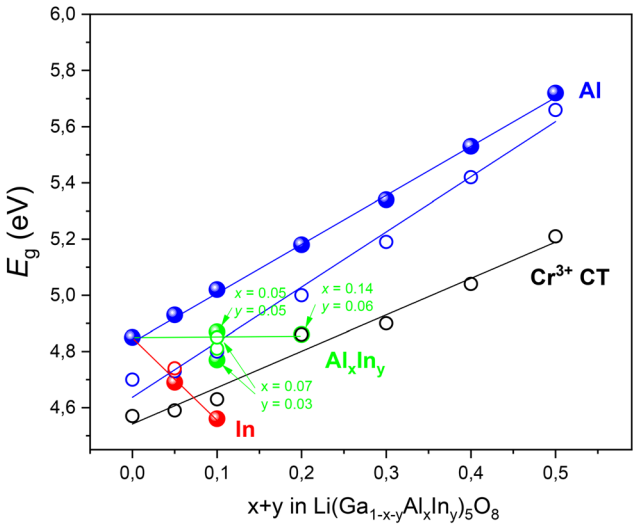

Fig. 9 Trends of the band gap energies of $Li(Ga_{1-x-y}Al_xIn_y)_5O_8$ alloys estimated from the calculated optical absorption spectra (solid symbols) and those estimated experimentally from the photoluminescence excitation spectra (open symbols) with the corresponding linear fittings.

the shift in the material band gap) is well consistent with that estimated from the calculated optical absorption spectra.

The photoluminescence spectra of the studied samples at room temperature (Fig. 11a) do not reveal any significant difference for the studied compositions of the host lattice. The PL spectrum features a narrow line at about 718 nm (deviating within 2 nm depending on the Al/In content) caused by the zero-phonon line (spin-forbidden $^2E \rightarrow {}^4A_2$ transition of Cr^{3+}) and vibronic sidebands originating from the same transition (see *e.g.*, the work of Hsu *et al.*).[13] The replacement of Ga by up to 50% of Al does not cause any noticeable changes in the room-temperature PL spectrum, while adding 5% of In increases somewhat a relative intensity of the vibronic sidebands around the 718 nm line. All the studied samples demonstrate the quantum efficiency (QE) of photoluminescence of about 50% except the samples with 5 and 10% of Al, for which a lower QE was revealed (Fig. 11b).

3.5. Temperature dependence of photoluminescence

The temperature evolution of the photoluminescence spectra of the studied samples is shown in Fig. 12. As it is seen from the figure, the narrow-line emission at 718 nm is superimposed on the broadband emission, which stretches from 600 to about 850 nm. This broadband emission, caused most likely by the spin-allowed $^4T_2(^4F) \rightarrow {}^4A_2$ transition of Cr^{3+}, became apparent at elevated temperatures. As shown in Fig. 12, the narrow-line emission at 718 nm is the only one present at temperatures much below room temperature and decreases in intensity as the temperature increases. Above 200 K, the broadband emission appears and grows, reaching its maximum at about 400 K, while the narrow-line emission disappears. The broadband emission quenches in turn at higher temperatures. Similar temperature behaviour of the $^2E \rightarrow {}^4A_2$ and $^4T_2(^4F) \rightarrow {}^4A_2$ emissions of Cr^{3+} has previously been reported, *e.g.*, for $Ga_2O_3:Cr^{3+}$, and is typical for Cr^{3+} centres in an intermediate crystal field strength when the ^2E and $^4T_2(^4F)$ emitting levels are in thermal equilibrium.[33]

Temperature dependences of the overall PL intensity of the studied samples are shown in Fig. 13, and the corresponding quenching parameters are presented in Table 3. It should be mentioned that the measured temperature dependence of the

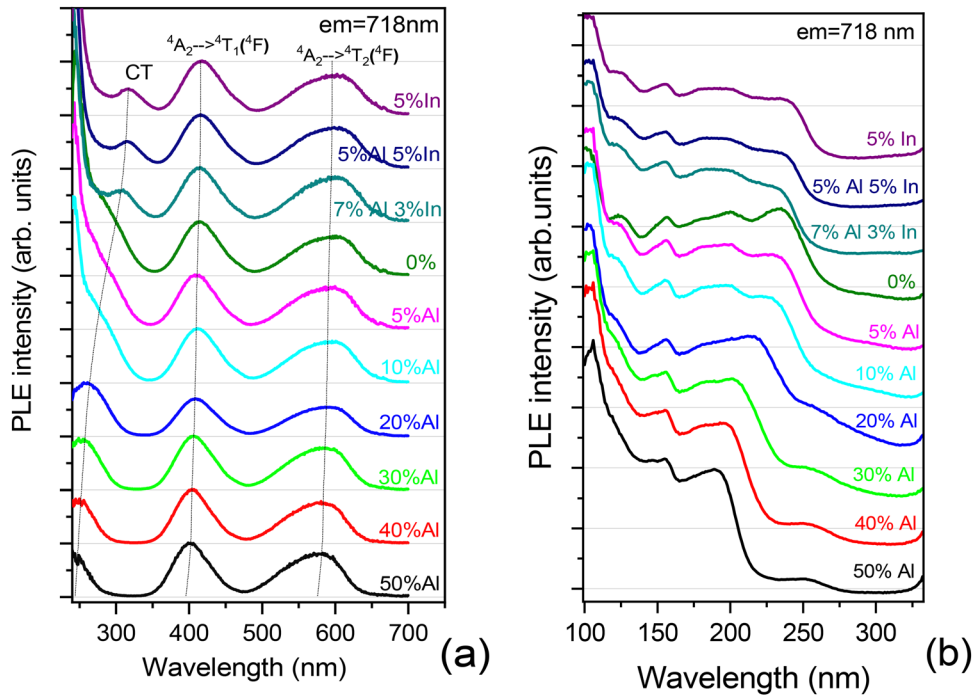

Fig. 10 Room-temperature photoluminescence excitation (PLE) spectra of the studied samples measured in UV-vis (a) and VUV-UV (b) ranges when recorded at 718 nm. The dotted lines demonstrating the peak positions are only a guide for the eyes.

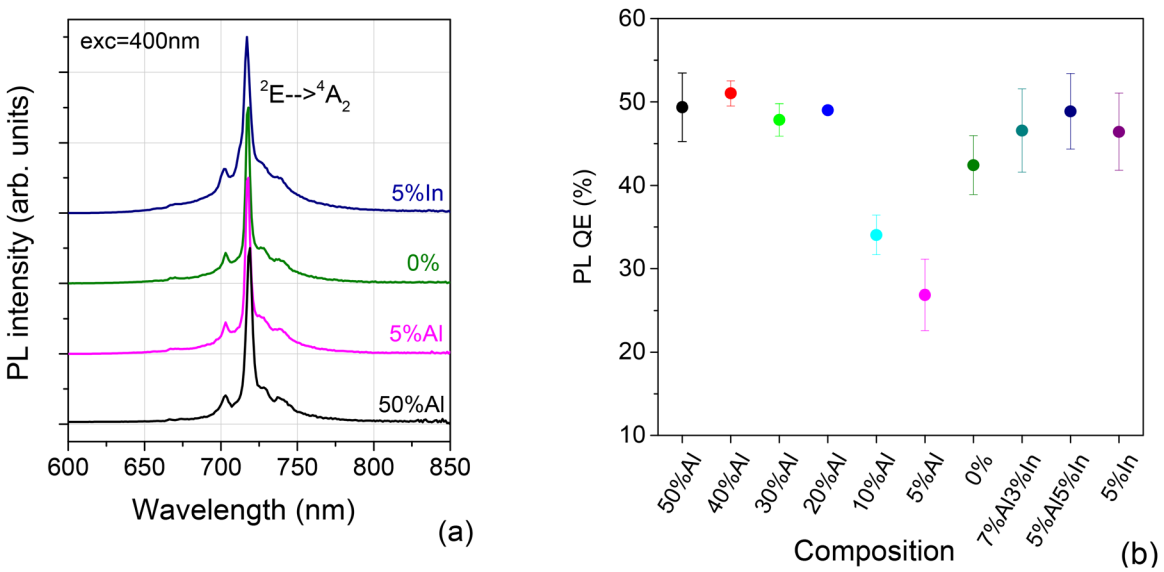

Fig. 11 Room-temperature photoluminescence (PL) spectra (a) and PL quantum efficiency (QE) (b) of the studied samples at 400 nm excitation.

PL intensity cannot be adequately fitted by the simplest quenching process:

$$I(T) = \frac{I(0)}{1 + A\exp\left(-\frac{E}{kT}\right)}, \quad (2)$$

where $I(0)$ is the emission intensity at zero temperature, ΔE is the activation energy of non-radiative transitions, and A is the ratio of the non-radiative transition probability to the radiative transition probability. To get more precise fitting of the experimental data, at least a two-step quenching model in accordance with Zhydachevskyy *et al.*[34] should be applied:

$$I(T) = \frac{I(0)}{1 + A_1\exp\left(-\frac{E_1}{kT}\right) + A_2\exp\left(-\frac{E_2}{kT}\right)}, \quad (3)$$

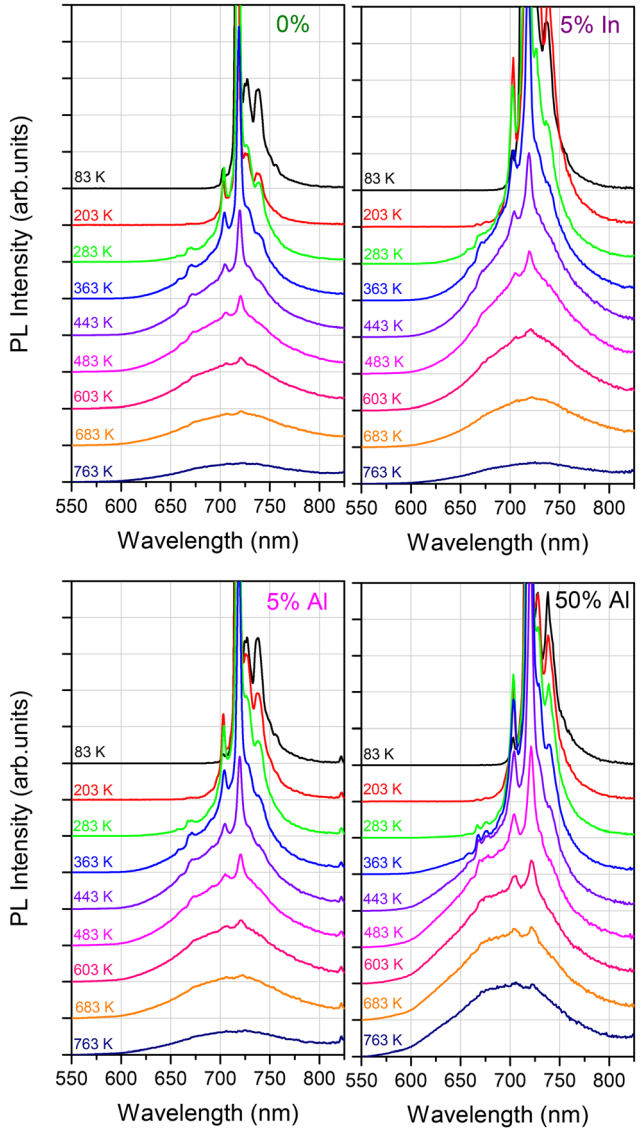

Fig. 12 Temperature evolution of the PL spectra of selected samples.

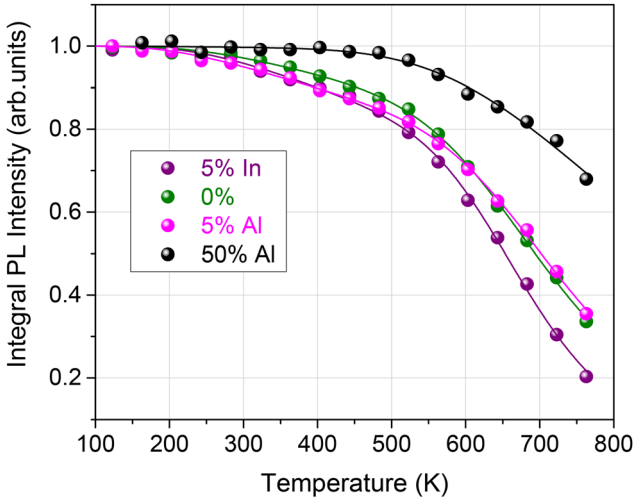

Fig. 13 Temperature dependence of the PL intensity of selected samples. The solid lines represent the fitting using eqn (3).

where ΔE_1 and ΔE_2 are the activation energies of two competing non-radiative pathways with the corresponding parameters, A_1 and A_2, related to the strength of the quenching processes. The presence of two competition quenching mechanisms seems obvious owing to at least two quenching processes observed experimentally; in particular, (i) the quenching of the narrow-line emission from the ^{2}E level by thermal population of the $^4T_2(^4F)$ level of Cr^{3+} and (ii) the thermal quenching of the emission from the $^4T_2(^4F)$ level itself. Besides, the possibility of multiple types of Cr^{3+} centres in the studied spinel host cannot be excluded as well.

As shown in Fig. 13 and Table 3, the quenching temperature $T_{\frac{1}{2}}$ decreases with the replacement of Ga by In, and increases when Ga is replaced by Al. It should be noted that the activation energy ΔE estimated in Hsu *et al.*[13] using the fitting with eqn (2) in a much narrower temperature range is in the middle of the ΔE_1 and ΔE_2 values obtained by us.

To get insight into the possibility of multiple Cr^{3+} centre formation in the studied compounds, a zero-phonon line (ZPL) emission originating from the $^2E \rightarrow {}^4A_2$ transition in the octahedrally-coordinated Cr^{3+} has been measured at liquid helium temperature. It is known that this emission is very sensitive to the local structure of the Cr^{3+} environment and their splitting (R-lines) can be used as a measure of the distortion of the CrO_6 octahedron.[35] Recently, it was shown that in the monoclinic $(Ga_{1-y}Al_y)_2O_3$ and $(Ga_{1-x}In_x)_2O_3$ solid solutions doped with Cr^{3+}, different distinct Cr^{3+} centres can be recognised in the ZPL, which were attributed to the Al-, Ga- and In-centred octahedra in this alloyed structure.[11] So it is of interest to check this for the spinel $Li(Ga_{1-x-y}Al_xIn_y)_5O_8:Cr^{3+}$ compounds studied here. As shown in Fig. 14, the $LiGa_5O_8$:Cr (0% Al) sample features a single and narrow ZPL at 716.7 nm. When Al is added, the same ZPL is observed; however, it gradually broadens and shifts towards longer wavelength as the Al content increases. When In is added, the same ZPL also broadens; however, it shifts in the opposite direction. It is also evident that for the In-containing samples, the line has got two additional components in the long- and short-wavelength sides of the main ZPL. Here, it should be noted that the additional ZPLs observed for the In-containing samples are not related to the second component (R_2-line) of zero-phonon emission from the possibly split ^{2}E level. Fig. 15 shows that the thermally populated R_2 component appears at the short-wavelength side of R_1 at temperatures above 60 K. It is noteworthy that the R_2 line for the In-containing compounds also has a multiple structure like R_1. It is also noteworthy that the ^{2}E level splitting (R_2–R_1 distance) for Cr^{3+} in $LiGa_5O_8$ is about 34.6 meV, which is twice as large as 18.2 meV for β-Ga_2O_3:Cr^{3+},[33] suggesting a larger distortion of Cr-centred octahedra (meaning the GaO_6 octahedra) in $LiGa_5O_8$ than in β-Ga_2O_3. It is also worth noting that the ^{2}E level splitting in $LiGa_5O_8$ increases gradually with increasing Al and In content

Table 3 Parameters of fits obtained from the temperature dependence of the emission intensity using eqn (3) for the studied $Li(Ga_{1-x-y}Al_xIn_y)_5O_8:Cr^{3+}$ compounds

Sample composition	ΔE_1, eV	ΔE_2, eV	A_1	A_2	$T_{\frac{1}{2}}$, K	ΔE^a, eV (ref. 13)
5% In	0.097 ± 0.001	0.61 ± 0.04	1.87 ± 0.7	$3.4 \times 10^3 \pm 2.5 \times 10^3$	653	—
0% Al	0.094 ± 0.017	0.49 ± 0.03	1.13 ± 0.51	$3.1 \times 10^3 \pm 1.6 \times 10^3$	694	0.123 ± 0.01
5% Al	0.078 ± 0.009	0.52 ± 0.03	1.08 ± 0.26	$4.2 \times 10^3 \pm 2.2 \times 10^3$	702	—
50% Al	0.055 ± 0.19	0.35 ± 0.05	0.02 ± 0.15	$1.0 \times 10^2 \pm 0.8 \times 10^2$	>800	—
60% Al	—	—	—	—	—	0.123 ± 0.004
100% Al	—	—	—	—	—	0.112 ± 0.04

[a] The ΔE value obtained from fitting by eqn (2) in the work of Hsu *et al.*[13]

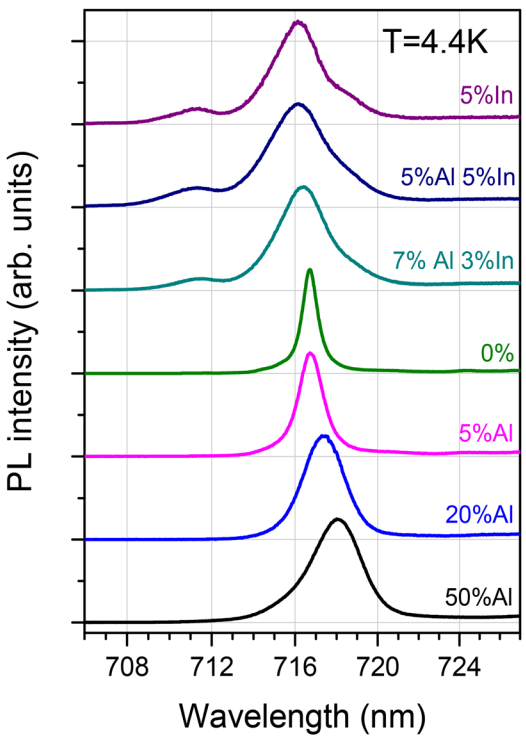

Fig. 14 High-resolution Cr^{3+} ZPL (R_1-line) emission spectra of the studied samples measured at T = 4.4 K.

(Fig. 15b), which is consistent with the bond length distortion in Ga octahedral positions presented in Fig. 4b.

3.6. Thermoluminescence after UV exposure

All the studied samples, after UV exposure to the CT band at about 270–310 nm (see Fig. 10), were revealed to possess quite efficient thermoluminescence below and above room temperature. Analysis of the TSL glow curves after UV exposure at a liquid nitrogen temperature, presented in Fig. 16a, reveals the following peculiarities. The thermoluminescence of pristine (non-modified by Al or In) $LiGa_5O_8$:Cr below and above room temperature is determined by the four main TSL peaks (marked as I, II, III and IV) with the peak maxima at about 120, 210, 350 and 500 K, respectively. Similar TSL peaks III and IV above room temperature were observed previously also for $LiGa_5O_8:Pr^{3+}$ (ref. 3), $LiGa_5O_8:Bi^{3+}$ (ref. 36), and $LiGa_5O_8:Tb^{3+}$ (ref. 1) synthesised using a similar high-temperature solid-state reaction method. This similarity suggests that these TSL peaks are related to the same kind of intrinsic point defect, at least when the material is synthesised in air using the solid-state method.

It is noteworthy that all samples modified by Al and/or In reveal a similar TSL structure; however, the position of the TSL peaks and their intensity ratios change. In particular, the position of all the TSL peaks shifts towards higher temperatures as the Al content increases, and *vice versa*, the TSL peaks move towards lower temperatures when the host is modified by In that is consistent with the results observed previously for γ-$(Ga_{1-x-y}Al_xIn_y)_2O_3$.[11] Additionally, as Al replaces Ga, the intensity ratio of the first two peaks (I and II) to the third and fourth peaks (III and IV) increases significantly.

The temperature range starting from room temperature to at least up to 100 °C (~374 K), which determines the room-temperature persistent luminescence, is marked in Fig. 16a. In such a way, it is obvious that the room-temperature persistent luminescence of $LiGa_5O_8$:Cr and compounds with small amounts of Al and In will be determined by TSL peaks III and IV, while, for compounds with larger amounts of Al, it will be determined already by peaks I and II. A precise comparison of the corresponding relative TSL intensities for different samples in this temperature range is shown in Fig. 16b.

It is also evident that simultaneously with changing the TSL peaks position, the modification of the $LiGa_5O_8$ host by the addition of Al and/or In makes the TSL peaks broader. The TSL peak broadening means an expansion of the set of trap depths caused by local structural disorder introduced by the partial replacement of Ga atoms with Al and/or In, see the work of Chang *et al.*[12] Assuming all other conditions (position of the peak and their intensity) are equal, the broadening of the TSL peaks themselves should result in more prolonged persistent luminescence of the material.

3.6.1. Effect of reducing annealing. Based on the belief that the radiation storage properties of the studied materials are caused by the oxygen-related intrinsic point defects (oxygen vacancies and interstitials), as reported by Jia *et al.*,[9] one can expect noticeable changes in TSL after the reducing thermal treatment of the materials synthesised in an oxidizing environment (*i.e.*, in air). Therefore, it is of interest to follow

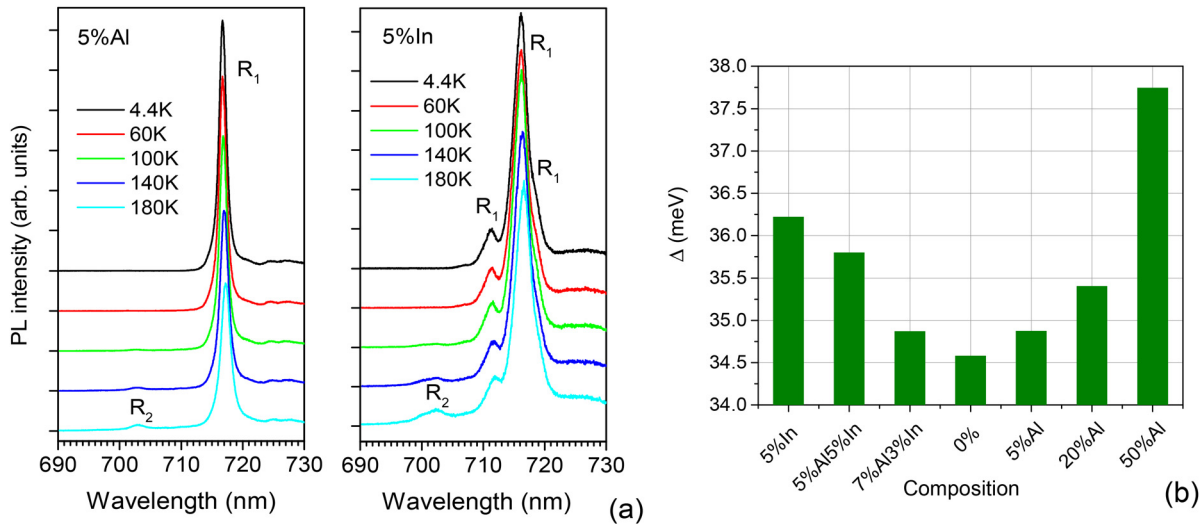

Fig. 15 Temperature evolution of the Cr^{3+} ZPL emission spectra of the 5% Al and 5% In samples (a) and the splitting of the ^2E level (R_2–R_1) of selected samples (b).

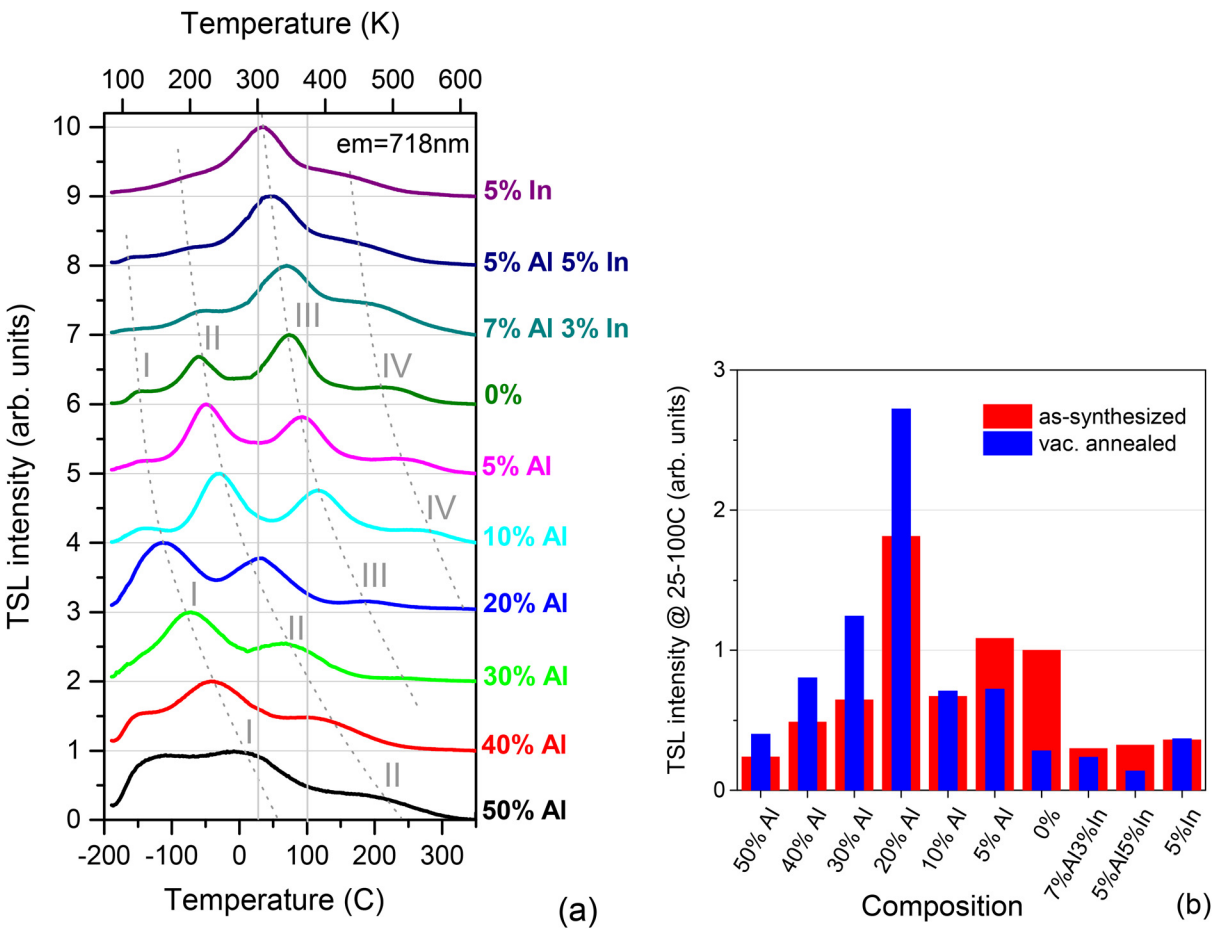

Fig. 16 Thermally stimulated luminescence (TSL) curves of the as-synthesised samples recorded at 718 nm after UV (270–310 nm) exposure at a liquid nitrogen temperature (a) and corresponding relative TSL intensities integrated in the temperature range from 25 to 100 °C for different (as-synthesised and annealed in vacuum) samples as a function of their composition (b). Heating rate: 1 C s^{-1}. The dotted lines demonstrating the peak positions are only a guide for the eyes.

the changes caused by the high-temperature annealing of the studied materials in a vacuum. The TSL curves of the samples after such annealing, compared to the as-synthesised samples, are shown in Fig. S6. As one can see from Fig. S6, the reducing annealing does not change the TSL structure; however, the relative and absolute intensities of certain peaks are changed. Specifically, the intensities of peaks III and IV are suppressed in all the studied samples, while those of peaks I and II usually increase, especially in the samples with a higher Al content. The increase in intensities of peaks I and II after annealing the samples with higher Al content is undoubtedly beneficial and should enhance their room-temperature persistent luminescence. The relative TSL intensities in the temperature range of 25–100 °C of the annealed samples are also shown in Fig. 16b. In such a way, the highest TSL intensity at 25–100 °C is observed for the 20% Al sample annealed in a vacuum, which reveals a threefold enhancement compared to the pristine $LiGa_5O_8$:Cr (0% Al) sample synthesised in air.

3.7. Persistent luminescence

After UV exposure to the CT band at about 270–310 nm, in the same way as TSL, the studied samples show an afterglow occurring in the deep-red spectral range corresponding to the Cr^{3+} emission in the materials. It should be noted that after exposure to visible light, including the 400 nm band, the afterglow is negligible. Fig. 17 shows a comparison of the room-temperature afterglow of selected samples after UV exposure. These results show good agreement with the TSL results presented above. In particular, samples containing 20% and 30% of Al reveal an enhanced PersL intensity compared to the pristine $LiGa_5O_8$:Cr (0% Al) sample, from which the 20% Al sample annealed under vacuum exhibits the highest PersL intensity.

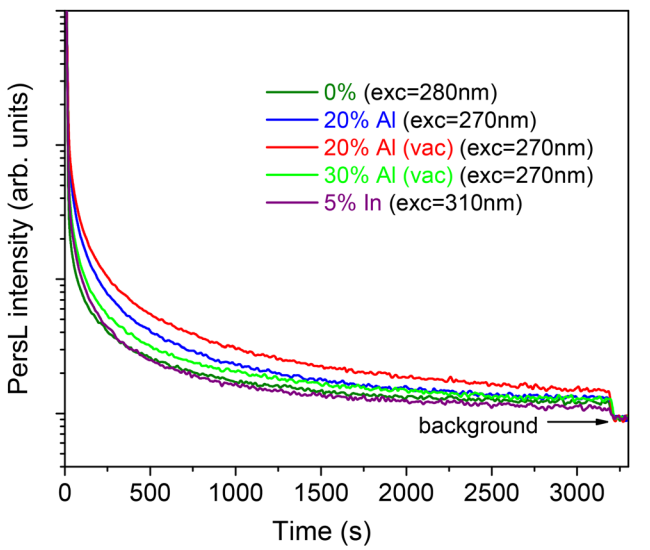

Fig. 17 Room-temperature afterglow decay kinetics of selected samples recorded at 718 nm after UV (270–310 nm) exposure.

4. Conclusions

All the $Li(Ga_{1-x-y}Al_xIn_y)_5O_8$ samples synthesised using the solid-state reaction method showed a pure cubic spinel structure. Only in the materials with nominal compositions $Li(Ga_{0.9}In_{0.1})_5O_8$ and $Li(Ga_{0.8}Al_{0.14}In_{0.06})_5O_8$ with relatively higher indium content, the traces of γ-$(Ga,In)O_3$ mixed oxide were detected.

Analysis of the average M–O distances within the MO_6 octahedra together with the Rietveld refinement suggests unambiguously that Al^{3+} ions prefer to occupy the octahedral 12*b* position (at least up to 50% of Al with respect to Ga), whereas larger In^{3+} cations mainly occupy the 8*c* Ga tetrahedral site. This suggestion has also been definitely confirmed by the DFT-based electronic structure calculations, as the Al_{Ga}[oct] and In_{Ga}[tetr] substituents protect against a noticeable increase in the total energy. The calculations also clearly reproduce the experimentally observed trends of the unit cell volume change as a function of Al or In content in the Li $(Ga_{1-x-y}Al_xIn_y)_5O_8$ alloys.

The calculations of the optical spectra of the lowest-energy $Li(Ga_{1-x-y}Al_xIn_y)_5O_8$ structures allowed us to evaluate the behaviour of the optical band gap depending on the cation composition of the compounds. In particular, the replacement of 50% of Ga by Al increases the E_g value of $LiGa_5O_8$ by almost 1 eV. Indium addition, in contrast, reduces the band gap, and this reduction is almost twice more pronounced: about 0.30 eV for 10% of In. This is well consistent with the edge of the band-to-band excitation estimated experimentally from the PLE spectra of Cr^{3+}.

The correlation between the lattice parameters (unit cell volume) and the band gap energy of the $Li(Ga_{1-x-y}Al_xIn_y)_5O_8$ samples is as follows: the smaller the unit cell volume in the $Li(Ga_{1-x}Al_x)_5O_8$ sample, the wider the band gap; conversely, the larger the unit cell volume in the $Li(Ga_{1-x}In_x)_5O_8$ sample, the narrower the band gap.

The photoluminescence spectra of $Li(Ga_{1-x-y}Al_xIn_y)_5O_8$:$Cr^{3+}$ phosphors at room temperature feature a narrow line emission at about 718 nm caused by the spin-forbidden $^2E \rightarrow {}^4A_2$ transition of the octahedrally coordinated Cr^{3+} and the corresponding vibronic sidebands. All the studied samples demonstrate the quantum efficiency (QE) of photoluminescence of about 50%, except the samples with 5 and 10% of Al, for which a somewhat lower QE was revealed.

The high-resolution, low-temperature photoluminescence measurements revealed a single type of Cr^{3+} centre in $LiGa_5O_8$:Cr. When Al is added, the same type of Cr^{3+} centre remains; however, the local structural disorder of the centres increases, which is evident in the broadening of the zero-phonon line (ZPL). When In is added, even greater (at the same amounts of In and Al) broadening of the ZPL is observed together with the appearance of two additional types of Cr^{3+} centres.

It was revealed that all the samples modified by Al and/or In show a similar TSL structure; however, the position of the TSL peaks and their intensity ratios change. In particular, the position of all the TSL peaks shifts towards higher tempera-

tures as the Al content increases, and *vice versa*, and the TSL peaks move towards lower temperatures when the host is modified by In, which is consistent with the modulation of the band gap of the host material. It was also shown that simultaneously with changing the TSL peak position, the modification of the $LiGa_5O_8$ host by the addition of Al and/or In makes the TSL peaks broader, which means an expansion of the set of trap depths caused by local structural disorder introduced by the partial replacement of Ga atoms with Al and/or In.

The highest TSL intensity in the temperature range of 25–100 °C was found for the $Li(Ga_{0.8}Al_{0.2})_5O_8$:Cr sample annealed under vacuum, which reveals a threefold enhancement of the persistent luminescence compared to that of the pristine $LiGa_5O_8$:Cr sample synthesised in air.

Author contributions

Anastasiia Karabut: visialization and investigation. Halyna Zhydachevska: sample synthesis. Łukasz Wachnicki: investigation. Vasyl Hreb: writing – review & editing, investigation, and visualization. Leonid Vasylechko: supervision, writing – review & editing, investigation, methodology, funding acquisition, resources, visualization, and writing – original draft. Yuriy Hizhnyi: writing – review & editing, investigation, and writing – origin draft. Tetiana Shevtsova: investigation. Andriy Luchechko: writing – review & editing and investigation. Agnieszka Pieniążek: investigation and writing – review & editing. Marek Berkowski: writing – review & editing and investigation. Yaroslav Zhydachevskyy: conceptualization, resources, funding acquisition, writing – original draft, and methodology. All authors have given approval to the final version of the manuscript.

Conflicts of interest

The authors declare no competing financial interest.

Data availability

The data supporting this article have been included as part of the supplementary information (SI). Supplementary information: graphical results of the Rietveld refinement of the selected $LiGa_5O_8$-based spinel structures, graphical results of the Rietveld refinement of chromium-doped $LaGa_5O_8$-based materials annealed under vacuum; concentration evolution of the lattice parameters and nearest cation–oxygen distances in the $Li(Ga_{1-x}M_x)_5O_8$ series; the 2 × 2 × 2 super-cell of the $LiGa_5O_8$ crystal; numbers of cationic substitutions modeled in the 2 × 2 × 2 super-cell of $Li(Ga_{1-x-y}Al_xIn_y)_5O_8$; DFT-optimised lattice parameters of $Li(Ga_{1-x-y}Al_xIn_y)_5O_8$ alloys; calculated low-energy parts of the absorption spectra of $Li(Ga_{1-x-y}Al_xIn_y)_5O_8$ crystals; comparison of the TSL curves of the studied samples (as-synthesised and annealed in a vacuum); PLE spectra of the studied samples obtained using synchrotron irradiation at room temperature (recorded at 718 nm), and their deconvolution into Gaussian peaks. See DOI: https://doi.org/10.1039/d6dt00337k.

Acknowledgements

This work was supported in part by the Polish National Science Centre (project no. 2024/53/B/ST11/01108), the Ministry of Education and Science of Ukraine (project DB/GALIO no. 0125U001768), the National Research Foundation of Ukraine (grant no. 2025.07/0218), and the European Research Executive Agency (HORIZON-MSCA-2023-SE-01 project no. 101182995). The authors gratefully acknowledge Polish high-performance computing infrastructure PLGrid (HPC Centre: ACK Cyfronet AGH) for providing computer facilities and support within the computational grant no. PLG/2024/017683. This work also received funding from the European Union through Project 101120397 – APPROACH. The assistance of Dr Oksana Chukova in taking measurements using synchrotron radiation is warmly acknowledged.

References

1 P. Zhang, X. Chen, Y. Bai, X. Zhao, X. Fu, L. Wu, Y. Wang, T. Sun, Y. Kong, Y. Zhang and J. Xu, Quasi-Continuous Defects Levels in Broadband Gap: A new strategy for high-temperature long persistent luminescence materials, *Opt. Mater.*, 2024, **12**, 2301406, https://advanced.onlinelibrary.wiley.com/doi/full/10.1002/adom.202301406.

2 X. Lu, Y. Wang, J. Yang, P. D. Townsend and D. Hreniak, $LiGa_5O_8:Fe^{3+}$: A novel and super long mear-infrared persistent material, *Ceramics International A*, 2024, **19**, 35359–35367, https://www.sciencedirect.com/science/article/abs/pii/S0272884224027822.

3 S. Wu, P. Xiong, K. Qin, Y. Xiao, B. Xiao, K. Chen, D. Jiang and Y. Wang, Ratiometric mechanoluminescence in single Pr^{3+}-actived $LiGa_5O_8$, *Luminescence*, 2023, **38**(8), 1465–1476, https://analyticalsciencejournals.onlinelibrary.wiley.com/doi/10.1002/bio.4528.

4 S. Lu, J. Wang and Q. Zhu, Differential substitution of Ga^{3+} by Mn^{2+} and Cr^{3+} in $LiGa_5O_8$ to prepare multi-mode fluorescent materials as array elements for anti-counterfeiting, *J. Alloys Compd.*, 2024, **1003**, 175567, https://www.sciencedirect.com/science/article/abs/pii/S0925838824021546?via%3Dihub.

5 N. I. Singh, L. L. Singh, A. N. Singh, L. R. Singh and S. B. Singh, Thermoluminescence analysis of NIR persistent phosphors (LGO:Cr) synthesized using sol-gel and solid-state methods, *J. Electron. Mater.*, 2024, **53**, 4848–4856, https://link.springer.com/article/10.1007/s11664-024-11208-4.

6 X. Yang, X. Zhang, Y. Hu, Y. Jia, Y. Wang, S. Yun and D. Gao, A phenomenological theory about effective after-

glow centers in persistent luminescence phosphors, *J. Alloys Compd.*, 2025, **1016**, 178893, https://www.sciencedirect.com/science/article/abs/pii/S0925838825004517?via%3Dihub.

7 K. Dabsamut, K. Takahashi and W. R. L. Lambrecht, Native defects and their complexes in spinel $LiGa_5O_8$, *J. Appl. Phys.*, 2024, **135**, 235707, https://pubs.aip.org/aip/jap/article/135/23/235707/3298664/Native-defects-and-their-complexes-in-spinel.

8 J. L. Lyons, Deep polaronic acceptors in $LiGa_5O_8$, *J. Appl. Phys.*, 2024, **135**, 165705, https://pubs.aip.org/aip/jap/article/135/16/165705/3285536/Deep-polaronic-acceptors-in-LiGa5O8.

9 M. Jia, X. Zhang, X. Yang, Z. Lin, D. Jia, Y. Wang, S. Yun and D. Gao, The self-activated $LiGa_5O_8$ storage phosphors: insights into its photo/thermo/mechano-stimulated NIR luminescence, *J. Mater. Chem. C*, 2025, **9**, 4616–4625, https://pubs.rsc.org/en/content/articlelanding/2025/tc/d4tc04818k.

10 Ya. Zhydachevskyy, Y. Hizhnyi, S. G. Nedilko, I. Kudryavtseva, V. Pankratov, V. Stasiv, L. Vasylechko, D. Sugar, A. Lushchik, M. Berkowski, A. Suchocki and N. Klyui, Band gap engineering and trap depths of intrinsic point defects in RAlO3 (R=Y, La, Gd, Yb, Lu) perovskites, *J. Phys. Chem. C*, 2021, **125**, 26698–26710, https://pubs.acs.org/doi/10.1021/acs.jpcc.1c06573.

11 V. Stasiv, Ya. Zhydachevskyy, V. Stadnik, V. Hreb, V. Mykhaylyk, L. Vasylechko, A. Luchechko, T. Wojciechowski, P. Sybilski and A. Suchocki, Chemical tuning of photo- and persistent luminescence of Cr^{3+}-actived β-Ga_2O_3 by alloying with Al_2O_3 and In_2O_3, *J. Alloys Compd*, 2024, **982**, 173827, https://www.sciencedirect.com/science/article/abs/pii/S0925838824004146.

12 C.-Y. Chang, N. Majewska, K.-C. Chen, W.-T. Huang, T. Lesniewski, G. Leniec, S. Kaczmarek, W.-K. Pang, V. Peterson, D.-H. Cherng, K.-M. Lu, S. Mahlik and R.-S. Liu, Ultrahigh quantum efficiency near-infread-II emission achieved by Cr^{3+} clusters to Ni^{2+} energy transfer, *Chem. Mater.*, 2022, **34**, 10190–10199, https://pubs.acs.org/doi/10.1021/acs.chemmater.4c00438.

13 J.-L. Hsu, R.-J. Chung, N. Majewska, D. Kreft, H.-S. Sheu, J.-F. Lee, S. Mahlik and M. H. Fang, Probing local structural changes by sharp luminescent infrared nanophosphors for application in light-emitting diodes, *Chem. Mater*, 2022, **34**, 11093–11100, https://pubs.acs.org/doi/10.1021/acs.chemmater.2c03224.

14 M. Kaminski, Y.-T. Tsai, Y.-L. Kuo, A. Mnnoz, U. R. Mendoza, M.-H. Fang and S. Mahlik, Exploring near-infrared luminescence of Ni^{2+} in $Li(Ga,Al)_5O_8$:spinels via mechanical and chemical pressure, *Chem. Mater*, 2026, **38**(2), 910–918, DOI: 10.1021/acs.chemmater.5c02959.

15 O. M. Sousa, Study of the structural, electronic, and optical properties of the host matrices of $LiAl_5O_8$ and $LiGa_5O_8$ via DFT, *Computational and Theoretical Chemistry*, 2018, **1123**, 96–101, https://www.sciencedirect.com/science/article/pii/S2210271X17304929.

16 O. M. Sousa and I. P. Carvalho, Theoretical study of the structural, energetic, electronic and magnetic properties of the host matrix $LiGa_5O_8$ doped with Cr^{3+}, *J. Solid State Chem.*, 2020, **289**, 121472, https://www.sciencedirect.com/science/article/abs/pii/S0022459620303029?via%3Dihub.

17 W. Lambrecht, Spinel $LiGa_5O_8$ prospects as ultra-wide-band-gap semiconductor: band structure, optical properties, and doping, *J. Vac. Sci. Technol., A*, 2024, **42**, 022705, https://pubs.aip.org/avs/jva/article/42/2/022705/3263554/Spinel-LiGa5O8-prospects-as-ultra-wideband-gap.

18 L. Akselrud and Y. Grin, WinCSD: software package for crystallographic calculations (Version 4), *J. Appl. Crystallogr*, 2014, **47**, 803–805, https://journals.iucr.org/paper?S1600576714001058.

19 Ya. Zhydachevskyy, I. Syvorotka, V. Tsiumra, M. Baran, L. Lipińska, A. Wierzbicka and A. Suchocki, Quantum efficiency of the down-conversion process in Bi^{3+}-Yb^{3+} and Ce^{3+}-Yb^{3+} co-doped garnets, *Sol. Energy Mater. Sol. Cells*, 2018, **185**, 240–251, https://www.sciencedirect.com/science/article/abs/pii/S0927024818302642?via%3Dihub.

20 Y. Smortsova, O. Chukova, M. Kirm, V. Nagirnyi, V. Pankratov, A. Kataev and A. Kotlov, The P66 time-resolved VUV spectroscopy beamline at PETRA III storage ring of DESY, *J. Synchrotron Radiat.*, 2025, **32**, 1539–1548, https://onlinelibrary.wiley.com/iucr/doi/10.1107/S1600577525007568.

21 BIOVIA Materials Studio, An Integrated, Multi-Scale Modeling Environment, https://www.3ds.com/productsservices/biovia/products/molecular-modeling-simulation/biovia-materials-studio, (accessed on 22 January 2025).

22 J. P. Perdew, K. Burke and M. Ernzerhof, Generalized gradient approximation made simple, *Phys. Rev. Lett*, 1996, **77**(18), 3865–2868, https://journals.aps.org/prl/abstract/10.1103/PhysRevLett.77.3865.

23 B. G. Pfrommer, M. Côté, S. G. Louie and M. L. Cohen, Relaxation of crystals with the quasi-Newton method, *J. Comput. Phys*, 1997, **131**, 233–240, https://www.sciencedirect.com/science/article/pii/S0021999196956120?via%3Dihub.

24 G. Kresse and D. Joubert, From ultrasoft pseudopotentials to the projector augmented-wave method, *Phys. Rev. B*, 1999, **59**, 1758–1775, https://journals.aps.org/prb/abstract/10.1103/PhysRevB.59.1758.

25 L. Vasylechko, V. Hreb, Ya. Zhydachevskyy, Y. Hizhnyi, A. Smaliuk, V. Stasiv, V. Stadnik, Y. Hirskyi, H. Zhydachevska, V. Mykhaylyk and A. Suchocki, Tuning of crystal structure and electronic band gap of the monoclinic Ga_2O_3 by simultaneous alloying with Al_2O_3 and In_2O_3, *Sci. Rep.*, 2025, **15**(1), 37128, https://www.nature.com/articles/s41598-025-21074-7.

26 A. Tomas, P. Laruelle, J. L. Dormann and M. Noguès, Affinement de la structure des formes ordonnée et desordonnée de l'octaoxopentaferrate de lithium, $LiFe_5O_8$, *Acta Crystallogr. C*, 1983, **39**, 1615–1617, https://journals.iucr.org/paper?a22819.

27 R. D. Shannon, Revised effective ionic radii and systematic studies of interatomic distances in halides and chalcogenides, *Acta Crystallogr., Sect. A:Found. Crystallogr.*, 1976, **32**, 751–767, https://journals.iucr.org/paper?S0567739476001551.

28 J. Joubert, M. Brunel, A. Waintal and A. Durif, Etude cristallographique du gallate de lithium et de sa solution solide avec l'aluminate, *C. R. Hebd. Seances Acad. Sci.*, 1963, **256**, 5324–5326, https://next-gen.materialsproject.org/materials/mp-28146.

29 S. Sasaki, C. T. Prewitt and R. C. Liebermann, The crystal structure of $CaGeO_3$ perovskite and the crystal chemistry of the $GbFeO_3$-type pervoskites, *Am. Mineral*, 1983, **68**, 1189, https://msaweb.org/AmMin/AM68/AM68_1189.pdf.

30 K. Zhang, V. G. T. Vangipuram, H.-L. Huang, J. Hwang and H. Zhao, Discovery of a robust p-type ultrawide bandgap oxide semiconductor: $LiGa_5O_8$, *Adv. Electron. Mater.*, 2025, **11**, 2300550, https://advanced.onlinelibrary.wiley.com/doi/10.1002/aelm.202300550?utm_medium=article&utm_source=researchgate.net.

31 P. Gluchowski and M. Chaika, Crystal-field strength variations and energy transfer of Cr^{3+} - doped GGG transparent nanoceramics, *J. Phys. Chem. C*, 2024, **128**, 9641–9651, https://pubs.acs.org/doi/10.1021/acs.jpcc.4c01658.

32 K. C. Chen, M. H. Fang, W. T. Huang, M. Kamiński, N. Majewska, T. Leśniewski, S. Mahlik, G. Leniec, S. M. Kaczmarek, C. W. Yang, K. M. Lu, H. S. Sheu and R. S. Liu, chemical and mechanical pressure-induced photoluminescence tuning via structural evolution and hydrostatic pressure, *Chem. Mater.*, 2021, **33**, 3832–3840, https://www.ch.ntu.edu.tw/~rsliu/publications/2021/12.pdf.

33 V. Mykhaylyk, H. Kraus, Ya. Zhydachevskyy, V. Tsiurma, A. Luchenchko, A. Wagner and A. Suchocki, Multimodal non-contact luminescence thermometry with Cr-doped oxidas, *Sensors*, 2020, **20**(18), 5259, https://www.mdpi.com/1424-8220/20/18/5259.

34 Ya. Zhydachevskyy, V. Mykhaylyk, V. Stasiv, L.-I. Bulyk, V. Hreb, I. Lutsyuk, A. Luchechko, S. Hayama, L. Vasylechko and A. Suchocki, Chemical tuning, pressure, temperature behavior of Mn^{4+} photoluminescence in Ga_2O_3-Al_2O_3 alloys, *Inorg. Chem.*, 2022, **65**, 18135–18146, https://pubs.acs.org/doi/10.1021/acs.inorgchem.2c02807.

35 M. Chaika, Temperature-depend spectroscopy of Cr^{3+}:YGG nanophosphors with multisite emission, *Mater. Res. Bull.*, 2025, **195**, 113841, https://www.sciencedirect.com/science/article/abs/pii/S0025540825005483?via%3Dihub.

36 Z. Yi, P. Liu, X. Liu and Y. Xu, Prolonged red persistent luminescence in Bi^{3+} single-doped $LiGa_5O_8$: regulating traps by site selective occupation, *Inorg. Chem.*, 2023, **62**, 19542–19551, https://pubs.acs.org/doi/10.1021/acs.inorgchem.3c02720.